Geochronology and glass geochemistry of major pleistocene eruptions in the Main Ethiopian Rift: Towards a regional tephrostratigraphy

Céline M. Vidal [a, b, *], Karen Fontijn [c], Christine S. Lane [a], Asfawossen Asrat [d, e], Dan Barfod [f], Emma L. Tomlinson [g], Alma Piermattei [a], William Hutchison [h], Amdemichael Zafu Tadesse [c], Gezahegn Yirgu [e], Alan Deino [i], Yves Moussallam [j], Paul Mohr [k], Frances Williams [l], Tamsin A. Mather [m], David M. Pyle [m], Clive Oppenheimer [a]

[a] Department of Geography - University of Cambridge, Downing Place, Cambridge, CB2 3EN, UK
[b] Fitzwilliam College, Storey's Way, CB3 0DG, UK
[c] Department of Geosciences, Environment and Society, Université Libre de Bruxelles, Av F Roosevelt 50 CP160/02, 1050, Brussels, Belgium
[d] Department of Mining and Geological Engineering, Botswana International University of Science and Technology, Private Bag 16, Palapye, Botswana
[e] School of Earth Sciences, Addis Ababa University, P. O. Box 1176, Addis Ababa, Ethiopia
[f] NEIF Argon Isotopes, University of Glasgow, SUERC, Scottish Enterprise Technology Park, Rankine Ave, Glasgow, G75 0QF, UK
[g] Department of Geology, Trinity College Dublin, The University of Dublin College Green, Dublin 2, D02 PN40, Ireland
[h] School of Earth & Environmental Sciences, Irvine Building, St Andrews, KY16 9AJ, UK
[i] Berkeley Geochronology Center, 2455 Ridge Road, Berkeley, CA, 94709, USA
[j] Lamont-Doherty Earth - Columbia University, Earth Observatory, 403 Comer, 61 Route 9W, Palisades, NY, 10964, USA
[k] 11 Tonagharraun, Corrandulla, Co. Galway, Ireland
[l] Department of Earth Sciences, University of Adelaide, Adelaide, 5005, Australia
[m] Department of Earth Sciences, University of Oxford, South Parks Road, Oxford, OX1 3AN, UK

ARTICLE INFO

ABSTRACT

The Main Ethiopian Rift (MER) is renowned as a focus of investigations into human origins. It is also the site of many large volcanic calderas, whose eruptions have spanned the timeframe of speciation, cultural innovation, and dispersal of our species. Yet, despite their significance for dating human fossils and cultural materials, the timing and geochemical signatures of some of the largest eruptions have remained poorly constrained at best. Here, through a programme of field surveys, geochemical analysis and $^{40}Ar/^{39}Ar$ dating, we report the ages of MER ignimbrites and link them to widespread tephra layers found in sequences of archaeological and paleoenvironmental significance. We date major eruptions of Fentale (76 ± 18 ka), Shala (ca. 145−155 ka), Kone (184 ± 42 ka and ca. 200 ± 12 ka) and Gedemsa (251 ± 47 ka) volcanoes, and correlate a suite of regionally important tephra horizons. Geochemical analysis highlights the predominantly peralkaline rhyolitic melt compositions (7.5−12 wt% Na_2O + K_2O, 70−76 wt% SiO_2) across the central MER and remarkable similarity in incompatible trace element ratios, limiting the correlation of deposits via glass composition alone. However, by integrating stratigraphic and geochronological evidence from proximal deposits, lake sediment cores and distal outcrops at archaeological sites, we have traced ash layers associated with the ca. 177 ka Corbetti, ca. 145−155 ka Shala and ca. 108 ka Bora-Baricha-Tullu-Moye eruptions across southern Ethiopia. In addition to strengthening the tephrochronological framework that supports paleoenvironmental and archaeological work in the region, our findings have wider implications for evaluating the hypothesis of a middle Pleistocene 'ignimbrite flare-up' in the MER, and for evaluating the impacts of these great eruptions on landscapes, hydrology, and human ecology.

© 2022 The Authors. Published by Elsevier Ltd. This is an open access article under the CC BY-NC-ND license (http://creativecommons.org/licenses/by-nc-nd/4.0/).

---

* Corresponding author. Department of Geography - University of Cambridge, Downing Place, Cambridge, CB2 3EN, UK.
E-mail address: cv325@cam.ac.uk (C.M. Vidal).

1. Introduction

More than two decades ago, Pyle (1999) highlighted the

potential to develop a tephrostratigraphic and tephrochronological framework for eastern Africa. Initially, much of the geochronological control for tephra deposits was obtained through conventional K–Ar dating, though in the last few decades single-crystal or small-population ^{40}Ar/^{39}Ar dating has been used to date both distal tephra horizons in archaeological contexts (e.g. in the MER, Brown and Fuller, 2008; Clark et al., 2003; Ian McDougall et al., 2005; Morgan and Renne, 2008), and proximal deposits (e.g. Hutchison et al., 2016a; Siegburg et al., 2018; Tadesse et al., 2022). Despite significant progress (Mana et al., 2018), we remain far from establishing a comprehensive tephra-based chronostratigraphic framework (Lane et al., 2017) for eastern Africa, as has been envisioned for Europe (e.g. Lowe et al., 2015). Such a framework will (i) greatly support and inform understanding of the interrelationships of large-scale climate variation with environmental and ecological change (including human evolution, migration and cultural innovation, e.g. Basell, 2008; Oppenheimer, 2011), and (ii) contribute to understanding of timescales and processes of magmatism and volcanism in the East African Rift System (EARS) and Afar. Improved dating, mapping and reconstruction of volcanic eruptions can also support investigations of their potential impacts on past human.

The Main Ethiopian Rift (MER, Fig. 1a) is a ~600 km long section of the EARS connecting the Afar Rift in northeastern Ethiopia to the Omo-Turkana Basin in the south (Corti, 2009). Along its central axis, it hosts regularly-spaced large silicic and smaller mafic volcanoes (Fontijn et al., 2018; Hunt et al., 2020; Mohr and Wood, 1976; Rooney et al., 2005, 2012). The largest Quaternary calderas in the MER are, from NE to SW, Fentale, the Kone-Birenti volcanic complex (KVC), the Boset-Baricha volcanic complex (BBVC), Boku, Gedemsa, Bora-Baricha-Tullu-Moye (BBTM), Aluto, Shala and Corbetti (Fig. 1b). Although probably Quaternary in age (Hutchison et al., 2016b, 2016c; Pyle, 1999; Woldegabriel et al., 1990), the timing and/or characteristics of the eruptions that formed them have been little studied (Fontijn et al., 2018; Hutchison et al., 2016b; Rampey et al., 2010; Siegburg et al., 2018; Tadesse et al., 2019, 2022). Significant post-caldera activity at these complexes includes eruptions of peralkaline rhyolitic magmas as obsidian flows, domes and pumice cones (Fontijn et al., 2018; Hunt et al., 2019; Tadesse et al., 2022). Only four Quaternary calderas (Fig. 1b) of the central MER complexes at Fentale (Williams et al., 2004), BBTM (Meki caldera, Tadesse et al., 2022), Aluto and Corbetti (Hutchison et al., 2016a) have been directly dated. This has suggested a middle Pleistocene clustering of major explosive eruptions in the MER, a so-called 'ignimbrite flare-up' (Hutchison et al., 2016a; Mohr et al., 1980) notably coinciding with the timeframe of occupation of the MER by both archaic humans and *Homo sapiens*.

Palaeoanthropological/archaeological studies routinely exploit the distal tephra record in building chronostratigraphies of sedimentary sequences containing fossils and artifacts. Although middle Pleistocene tephra in such settings are described in the literature, only a couple of robust correlations have been made with any of the large magnitude explosive eruptions of the MER (Vidal et al., 2022). Efforts to correlate deposits based on geochemistry have been hindered by a lack of standardisation of analytical protocols (e.g., in electron microprobe analytical conditions such as accelerating voltage, beam current and beam diameter) precluding straightforward intercomparison of reported geochemical fingerprints of individual deposits. However, developments in analytical techniques and the discovery of further promising stratigraphic sequences may redress these issues (e.g. Kuehn et al., 2011; Lowe et al., 2017; Pearce and Abbott, 2014; Tomlinson et al., 2010a, 2010b).

As a contribution to building a tephrochronology for eastern Africa, here we combine existing glass geochemistry and geochronological datasets with new tephrochemistry and radiometric ages

of proximal deposits as well as geochemical analyses of distal tephra layers in archaeological contexts of late middle Pleistocene strata and lacustrine core records. While the stratigraphy of each volcanic complex is described in the literature (Fontijn et al., 2018; Hunt et al., 2019; Hutchison et al., 2016a; Mohr et al., 1980; Rampey et al., 2010; Tadesse et al., 2019, 2022), we focus here on (co-) ignimbrite deposits from large magnitude eruptions of Fentale, KVC, Gedemsa, and Shala, as well as distal tephra in middle-to-late Pleistocene sedimentary archives, including the Omo-Kibish (Brown et al., 2012; Brown and Fuller, 2008; McDougall et al., 2005) and Gademotta-Kulkuletti formations (Laury and Albritton, 1975; Morgan and Renne, 2008; Sahle et al., 2014), and the Chew Bahir sediment core (Foerster et al., 2012, 2018; Trauth et al., 2018, 2019; Viehberg et al., 2018). We review existing datasets, report new age and geochemical data, and discuss the tephrochronological significance of these findings.

2. Overview of the late middle pleistocene calderas and ignimbrites in the MER

With the exception of Shala, the eruptive history of the Quaternary peralkaline volcanic complexes of the MER has been recently (re)investigated. These recent studies do not systematically include ^{40}Ar/^{39}Ar ages or glass trace element data. In the following, we review briefly the geologic background for each caldera and information available for their associated ignimbrites. We note here that ignimbrites are not necessarily associated with caldera formation as observed at peralkaline systems elsewhere (e.g. Romano et al., 2022). The occurrence of several ignimbrites at one system (e.g. at KVC, BBTM, Aluto, Shala) therefore makes difficult the attribution of an ignimbrite to a caldera unless the proximal stratigraphy is clear.

The northernmost MER caldera is 3 km by 4.4 km, belonging to Fentale volcano (Fig. 1b; Hunt et al., 2019). The caldera-associated ignimbrite extends across the plain surrounding the edifice up to ~12 km from the summit (Gibson, 1970; Hunt et al., 2019; Williams et al., 2004). Previous fission track dating of the characteristic green, welded ignimbrite yielded an age of 168 ± 38 ka (Williams et al., 2004).

The Kone-Birenti Volcanic Complex (KVC) hosts at least three nested calderas previously described by Cole (1969) and Rampey et al. (2014, 2010). The oldest is the ~11-km-diameter Birenti caldera, whose eastern and southern rims are readily discerned, is associated with ignimbrites Qub and Qpb (Rampey et al., 2010). The younger 5 km by 6 km Kone caldera (Fig. 1b) is associated with the Qpk ignimbrite (Rampey et al., 2010). The 1.5 km by 2 km Korke embayment is located to the east of the Kone caldera (Cole, 1969; Rampey et al., 2010). Major element compositions of the Qpk Kone ignimbrite were recently analysed by Fontijn et al. (2018).

The Boset-Bericha Volcanic Complex (BBVC) is one of the largest stratovolcanoes of the northern MER, comprising two edifices, Gudda and Bericha (Siegburg et al., 2018). The eruptive history was first documented by Brotzu et al. (1974) and Di Paola (1972) and recently reviewed by Siegburg et al. (2018). A remnant caldera rim of the Gudda edifice suggests that the original caldera diameter is ca. 4 km. Pumice lapilli deposits sampled near the rim are dated ca. 120 ± 6 ka, and would predate or have formed during the caldera-forming eruption (Siegburg et al., 2018).

The Boku volcanic complex (BVC) is located SE of Adama (Fig. 1b), and hosts a caldera associated with a welded ignimbrite, Qpw, first described by Boccaletti et al. (1999). A recent reinvestigation of the eruptive history and magmatic evolution of BVC suggested that the caldera would have formed between ca. 510 ka and ca. 830 ka, according to correlations of proximal deposits with the primary regional units (Tadesse et al., 2019). The
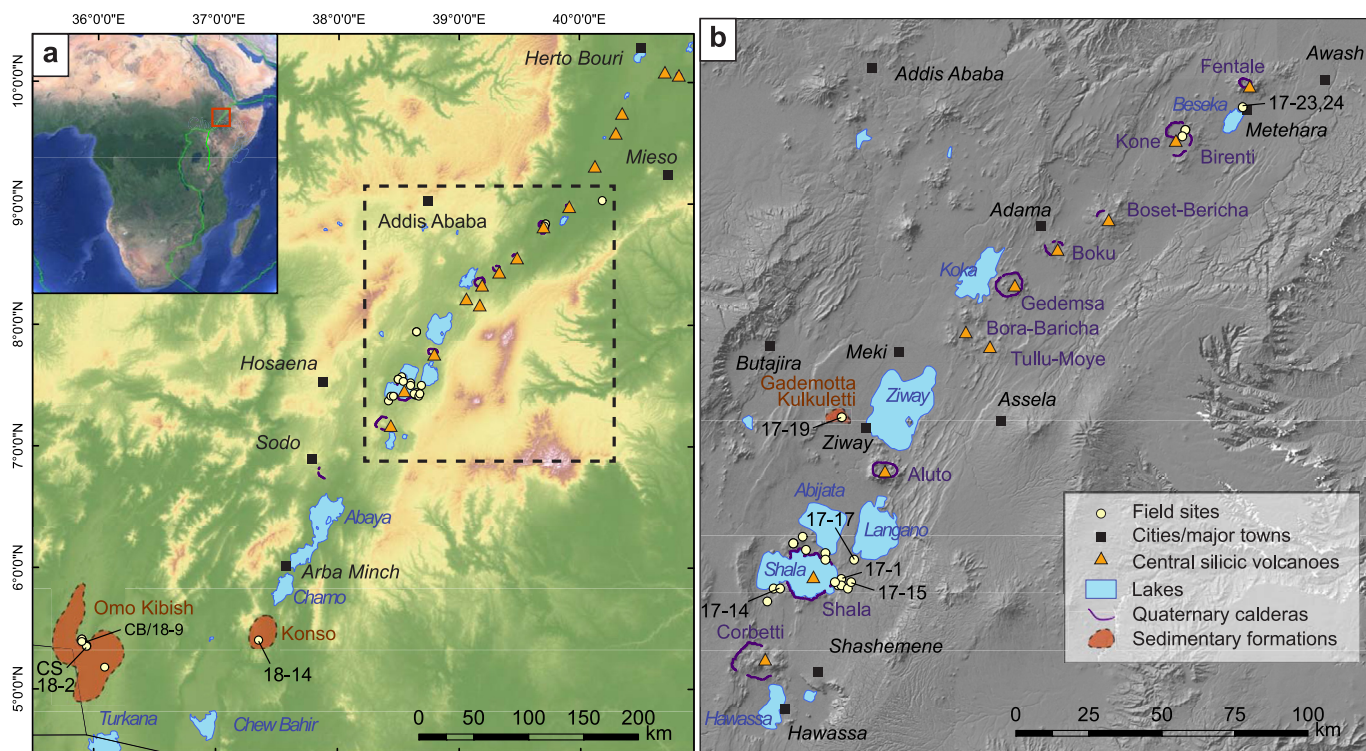
Fig. 1. a Map of the Main Ethiopian Rift (MER) and **b** enlargement of the MER showing central silicic volcanoes and field sites. Field site numbers as per Table 1, prefix 'ETH' omitted for brevity. Sources are Shuttle Radar Topography Mission Digital Elevation Model data at one arcsecond resolution from the NASA Land Processes Distributed Active Archive Center Products (https://earthexplorer.usgs.gov/); settlements, lakes, and topography were obtained from (https://www.naturalearthdata.com/).

microcrystalline structure of groundmass glass in the ignimbrite has precluded major and trace element analysis of the glass.

The Gedemsa volcanic system comprises a 7.3 km by 9.6 km caldera (Hunt et al., 2019, Fig. 1b) and sequences of unwelded ignimbrites likely emplaced during caldera formation (Fontijn et al., 2018; Peccerillo et al., 2003; Thrall, 1973). Using a digital elevation model (DEM) and deposit thickness, Hutchison et al. (2016a) calculated the total volume of silicic magma produced during the caldera collapse of Gedemsa to range from 14 to 31 km^3 DRE (Dense Rock Equivalent). Peccerillo et al. (2003) dated post-caldera lavas at 265 ± 20 ka and pre-caldera obsidian at 319 ± 20 ka, suggesting that the current well-expressed caldera formed between ca. 339 and ca. 245 ka. Pumice samples from the same eruption cluster associated with the caldera formation were described and analysed for glass major element composition by Fontijn et al. (2018).

The Bora-Baricha-Tullu Moye (BBTM) volcanic system comprises three main silicic edifices, Bora, Baricha and Tullu Moye, and numerous smaller vents (including Oda and Werdi). Following early descriptions of the deposits (Bizouard and Paola, 1978; Di Paola, 1972), Fontijn et al. (2018) provided a preliminary stratigraphic sequence for BBTM, further investigated by Tadesse et al. (2022). In the latter study, Tadesse et al. (2022) identified and analysed the composition of two major deposits associated with large-magnitude, and possibly caldera-forming eruptions: the 108 ± 9 ka Meki deposit, which overlies the older Suke ignimbrite. The latter could not be dated due to the lack of datable material (Tadesse et al., 2022).

The Aluto volcanic complex is one of the restless silicic peralkaline volcano of the MER (Biggs et al., 2011; Hutchison et al., 2016a), located south of lake Ziway (Fig. 1b). A ~1 km long segment of caldera wall visible on the north-east of the complex first suggested one or more caldera-forming events at Aluto (Dakin and Gibson, 1971). Hutchison et al. (2016b) later identified a 8 by

5 km wide collapsed caldera structure associated with welded ignimbrite units Qgei and Qgyi at overlapping ^{40}Ar/^{39}Ar ages of 316 ± 13 ka and 306 ± 12 ka. Hutchison et al. (2016a) calculated a caldera volume of 8−21 km^3 DRE. Field evidence was insufficient to assess whether the ignimbrites represent one or multiple eruptive events, however these deposits represent the best candidates for widely dispersed, explosive ignimbrite sheets associated with a classic peralkaline caldera collapse. The welded nature of the deposits has precluded geochemical fingerprinting of the matrix glass.

The Shala volcanic complex, previously referred to as O'a caldera (Mohr et al., 1980) is characterised by a 15-km-wide caldera occupied by a 250-m-deep lake (Fig. 1b) (Baumann et al., 1975; Le Turdu et al., 1999). This is the largest Pleistocene caldera recognised in the MER, with a total caldera-forming eruption volume of 86−170 km^3 DRE (Hutchison et al., 2016a), but notable for the absence of major resurgent activity within the caldera, based on a bathymetric profile of Lake Shala (Le Turdu et al., 1999). The most recent activity is evident NW of the lake at a stratocone, Tullu Fike; SW of the lake at Chitu maar; and several basaltic scoria cones, found N and S of the caldera (Mohr et al., 1980). Reported the size (volume) of the caldera as 86−170 km^3 DRE. The Quaternary Shala eruptive sequence exposed around the lake. Mohr et al. (1980) first described the youngest caldera-forming eruption deposits, represented by ignimbrites Qi4a, Qi4b and Qi5 (Fig. 2b, d, e), which are best preserved E of the lake (Mohr et al., 1980). We dated and analysed ignimbrites Qi4a (sample E76/50), and Qi5 (sample E76/61) of Mohr et al. (1980). Pumice fallout Qr2a overlying ignimbrite Qi5 (Fig. 2c) was interpreted as a product of post-caldera activity, possibly associated with the Tullu Fike cone (Mohr et al., 1980). An older ignimbrite, Qi2 (Mohr et al., 1980) cropping SW of the lake was recently dated at 233 ± 22 ka (Vidal et al., 2022). Qi2 and Qi4a ignimbrite are separated by pumice fallout deposits Qi3, which are

possibly the products of an eruption of Corbetti, since they only crop out SW of Lake Shala (Mohr et al., 1980).

The Corbetti volcanic complex comprises a 10.9 by 15.6 km wide collapsed caldera structure (Hunt et al., 2019) which hosts the two post caldera centres Chabbi and Urji (Hutchison et al., 2016b; Mohr, 1966; Rapprich, 2016). A welded ignimbrite (COI2E) attributed to the caldera formation of Corbetti is dated 177 ± 8 ka (Hutchison et al., 2016b). The size of the caldera represents a total volume of 25−63 km^3 DRE (Hutchison et al., 2016a), and stands as the second largest Quaternary caldera of the central MER. Analyses of major and trace elements of glasses from the ca. 177 ka COI2E ignimbrite revealed a correlation with tuff TA-56 of the Konso formation, in the southern MER (Fig. 1, Vidal et al., 2022).
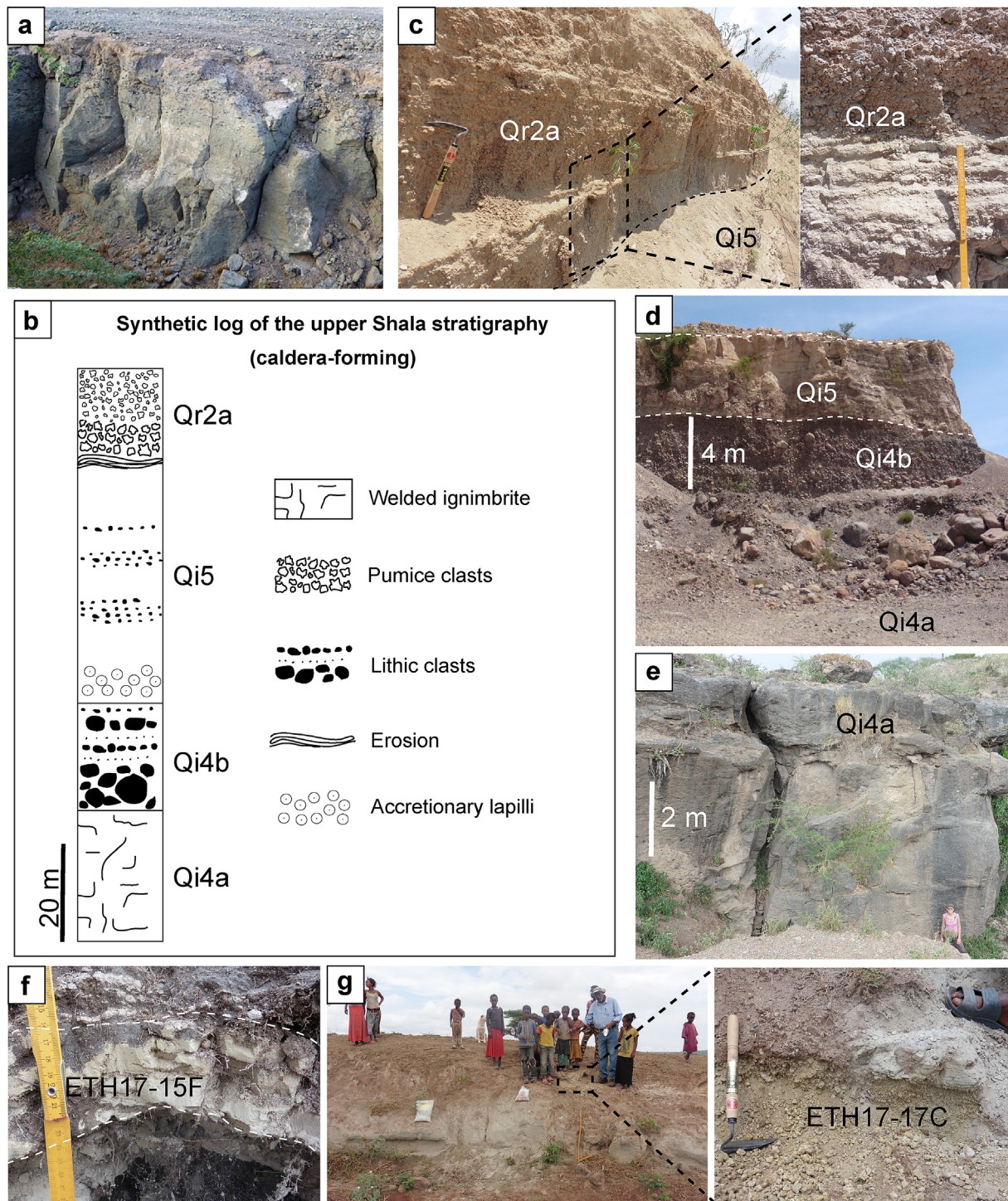
Fig. 2. New proximal samples. a Fentale ignimbrite at site ETH17-24 (Fig. 1b). **b** Synthetic stratigraphic log of the upper Shala stratigraphy associated with the caldera-forming phase (Mohr et al., 1980). **c** and **d** Shala deposits at site ETH17-1 (Fig. 1b). **e** Welded ignimbrite Qi4a from Shala at site ETH17-2. **f** Fallout deposit at site ETH17-15 (Fig. 1b) and **g** Deposits at site ETH17-17 (Fig. 1b), probably associated with Shala.

3. Methods

3.1. Fieldwork

In 2017 and 2018, we sampled the Fentale ignimbrite, proximal units of the upper stratigraphy of Shala (Mohr et al., 1980), and revisited the Gademotta-Kulkuleti and Kibish Formations (Fig. 1a) to sample all known middle-to-late Pleistocene tephra horizons. At each site we described the stratigraphy, measured sections (with particular attention to tephra horizons) and sampled well exposed and least altered tephra. Ignimbrites samples from KVC, and Gedemsa were samples during campaigns in 2015 and 2017 described in Fontijn et al. (2018). Samples studied here were collected across several field seasons, resulting in different identification systems. Details of new samples and field observations are reported in section 4.

3.2. $^{40}Ar/^{39}Ar$ dating

We prepared welded ignimbrite, pumice and ash samples at the Department of Geography, University of Cambridge and at the Department of Earth Sciences, University of Oxford. Rocks were pulverised in a jaw crusher and sieved to $250-500$ μm size fraction, cleaned in water, and passed through a Frantz magnetic barrier laboratory separator to isolate sanidine phenocrysts from groundmass. Because separates still contained other non- or very weakly magnetic phases (primarily glass and quartz), 100 to 200 inclusion-free sanidine grains were handpicked, then leached in 5% HF to remove any adhering glass.

Samples and neutron flux monitors were packaged in aluminium discs and stacked in quartz tubes for later reconstruction of neutron flux gradients. The sample package was irradiated in the Oregon State University reactor, Cd-shielded facility. Alder Creek sanidine (1.1891 ± 0.0008 (1σ) Ma, Niespolo et al., 2017) was used to monitor ^{39}Ar production and establish neutron flux values (J) for the samples. Gas was extracted from samples via heating with a mid-infrared (10.6 μm) CO_2 laser employing a non-gaussian, uniform energy profile and a 2.0 mm beam diameter centred over a sample well. The samples were housed in a doubly-pumped ZnS-window laser cell and loaded into a stainless steel planchette containing 208 2.0 mm diameter wells. Liberated argon was purified of active gases, e.g., CO_2, H_2O, H_2, N_2, CH_4, using two Zr−Al getters; one at 16 °C and two at 400 °C. Data were collected on a Mass Analyser Products MAP-215-50 single-collector mass spectrometer using an electron multiplier collector in dynamic collection (peak hopping) mode. Time-intensity data were regressed to inlet time with linear or second-order polynomial fits to the data. The average total system blank for laser extractions, measured between sample runs, was $1.1 \pm 0.6 \times 10{-}15$ mol ^{40}Ar, $1.6 \pm 0.7 \times 10^{-17}$ mol ^{39}Ar, and $7.4 \pm 3.2 \times 10{-}18$ mol ^{36}Ar. Mass discrimination was monitored daily, between and within sample runs by analysis of an air standard aliquot delivered by an automated pipette system. All blank, interference and mass discrimination calculations were performed with the MassSpec software package (MassSpec, version 8.16, authored by Al Deino, Berkeley Geochronology Center).

Grain analyses with <10% radiogenic gas, negative ages or ages in excess of 1 Ma were omitted. Peak age distributions were then defined by determining the youngest population or most contiguous group of individual grain analyses that conforms to a gaussian distribution with the expected scatter as indicated by the value of Mean Square Weighted Deviate (MSWD). Samples FEN1 and FEN2 show anomalously low MSWD relative to the number of individual analyses (n), suggesting an overestimate of analytical uncertainties.

However, various approaches to filtering the data generally resulted in MSWD below 0.7, which approximates the expected minimum for the large number of grains analysed. For these analyses, the bulk of the age uncertainty derives from the measurement of ^{36}Ar.

Raw data are reported in Table S1 and plots in supplementary figures S1−S7.

3.3. Ignimbrite and distal tephra sample preparation for geochemical analysis

Pumice clasts and welded ignimbrite samples of the Fentale, Kone, and Shala (Table 1, Fig. 1b) were crushed, sieved at 500, 250, and 125 μm, and washed in purified water and hydrochloric acid (1%) in an ultrasonic bath. Distal tephra samples (Table 1) from the Gademotta, and Kibish Formations were washed through an 80 or 25 μm sieve in purified water. Glass grains from 125 to 250 μm and 250−500 μm fractions were handpicked and mounted in epoxy resin stubs and polished. Samples of smaller grain size fractions were mounted directly in stubs.

3.4. Extraction and mounting of cryptotephra from the Chew Bahir core

During core opening and description, ash-bearing zones within core sections were noted and sedimentary features described. Smear slides were used to define the core depth range exhibiting high concentrations of glass shards. Continuous and contiguous 10 cm samples were taken along the same interval to quantify the abundance of shards using standard cryptotephra methods (Blockley et al., 2005; see Supplementary Information section 2, Tephrochronology). Tephra layers were given site-specific codes, indicative of either their first appearance or sample mid-point depth in the composite core record, i.e. "CHB_T (depth m)".

Samples containing tephra were washed through a sieve at 25 μm to remove fine material, before being mounted in epoxy resin on a microprobe sample stub. Epoxy stub mounts were ground by hand to expose glass shards in horizontal cross section and then polished in multiple steps using diamond paste to a 0.25 μm grade.

3.5. Major element analysis

Individual glass shards were analysed with an SX100 CAMECA electron microprobe (EMPA) at the Department of Earth Sciences, University of Cambridge, UK. Major elements were measured with an accelerating voltage of 15 keV, 10 nA and a 10-μm diameter defocused beam. Elements were counted on-peak for 10 s (Na, Si), 20 s (Al, Fe and K), 60 s (Ti, Mg, Ca, and Cl), 90 s (P) and 120 s (Mn). Sodium was measured first to minimise alkali loss. The analytical accuracy was checked against international standards ATHO-G, STHS6, VG-568 and an internal standard of peralkaline obsidian from Lipari (74 wt% SiO_2, 3.8 wt% Na_2O, 5.3 wt% K_2O). Compositions of the standards and standard deviations are reported in Table S2. Where possible, we analysed 30−50 points per sample. Normalised compositions are reported in Table S3. Analytical procedures for samples from Gedemsa and KVC are explained in Fontijn et al., (2018).

3.6. Data treatment

Outcrop samples exposed in tropical arid and semi-arid environments typically experience pedogenesis or other forms of weathering or alteration, reducing alkali (Na_2O and K_2O) contents.

Table 1
Volcanic source, type, location and single crystal^{40}Ar/^{39}Ar ages of ignimbrite and tephra samples.

Volcano	Unit	Sample	Rock type	Sampling site	Longitude (E)	Latitude (N)	Elevation (m)	Single grain population age (Ka)	±2s w/J (Ka)	MSWD	p	n
Proximal samples												
Fentale	NA (caldera)	FEN1	Welded ignimbrite	ETH17-24	39.908117	8.905733	971	0.097	0.029	0.54	0.96	24
	NA (caldera)	FEN2	Welded ignimbrite	ETH17-25	39.903317	8.92265		0.064	0.022	0.26	1.00	57
		Composite						0.076	0.018	0.38	1.00	81
Kone	Qpk	MER 132 A	Pumice (ignimbrite)	MER132	39.722	8.838	1333	0.199	0.017	1.20	0.16	51
	Qpk	MER 140B/MER 139 A	Pumice (ignimbrite)	MER140	39.733	8.843	1255	0.200	0.016	1.27	0.11	44
		Composite						0.200	0.012	1.22	0.07	95
	Qpk?Qpb?	MER 141 A	Pumice (ignimbrite)	MER141	39.737	8.846	1262	0.184	0.042	0.82	0.74	29
Gedemsa	NA (caldera)	MER 080B/084 A	Pumice (ignimbrite)	MER080, MER077, MER084 (1)			0.240	0.130	0.36	0.7	3	
	NA (caldera)	MER 077B/084 A	Pumice (ignimbrite)	MER080, MER077, MER084 (1)			0.253	0.051	1.39	0.25	3	
		Composite						0.251	0.047	0.71	0.62	6
Shala	Qr2a	ETH17-1QR2A	Pumice (tephra)	ETH17-1	38.647453	7.449137	1762	0.155	0.020	0.87	0.67	30
	Qi5	E76/61	Pumice (ignimbrite)	ETH17-1	38.647453	7.449137	1762	0.155	0.014	0.93	0.61	49
	Qi4	E76/50	Welded ignimbrite	ETH17-1	38.647453	7.449137	1762	0.145	0.011	0.99	0.48	41
	NA	ETH17-15 F	Pumice (tephra)	ETH17-15	38.669355	7.416478	1840					
	NA	ETH17-17C,D	Pumice (tephra)	ETH17-17	38.687983	7.507372	1790					
Distal samples Archive												
Kibish F.	Alyio tuff	ETH18-2/ETH18-9 A	Tuff	ETH18-02	35.935784	5.347604	472.61					
Kibish F.		ETH18-09C	Tuff	ETH18-09	35.936084	5.363468	418.06					
		ETH18-09D	Tuff	ETH18-09	35.936084	5.363468	418.06					
Gademotta F.	Unit 15	ETH17-19	Primary tephra	ETH17-19	38.645997	7.946485	1886	0.135	0.020	0.66	0.98	60
Chew Bahir core	CHB_T86.70	CT648	Cryptotephra									

Compositions were normalised to 100 wt% volatile-free (Lowe, 2011), and compared using bi-plots and principal component analysis. Owing to the alkali-rich nature of the MER samples, most of the analyses had totals under 94 wt%. Sodium loss was checked by plotting un-normalised Na_2O concentrations against totals. Analyses with analytical totals <92 wt% yielded erroneously high SiO_2 and Al_2O_3 concentrations, and were discarded.

3.7. Trace element analysis

Trace element compositions of individual tephra shards were analysed by LA-ICP-MS at the iCRAG laboratory at Trinity College Dublin. The instrument used was a Thermo iCAPQ coupled to a Photon Machines G2 193 nm excimer laser and a HelEx two volume cell. We used a spot size of 24 or 30 μm, depending on shard morphology and size, a repetition rate of 6 Hz, and a count time of 33 s (200 pulses) on the sample and 30 s on the gas blank (background). Concentrations were calibrated using NIST612 with ^{29}Si as the internal standard. Data reduction was undertaken using the Iolite software and a secondary Ca correction factor was applied following Tomlinson et al. (2010a, 2010b). Precision of ATHO-G and StHs6/80-G MPI-DING glass secondary standard analyses is typically better than 6% for most elements (Table S4). Where possible, we analysed 15−25 glass shards per sample. Compositions are reported in Table S5.

4. Samples and new stratigraphies

Here we describe the samples analysed for each volcano, field sites and our new stratigraphic observations. A list of samples with location information is provided in Table 1.

4.1. Proximal samples

4.1.1. Fentale

We collected two samples (FEN1 and FEN2, Table 1) of the green welded ignimbrite of the caldera-forming eruption of Fentale, 5−8 km south of the caldera (Fig. 2a), at sites ETH17-23 and ETH17-24, NW of Metehara (Fig. 1b) for redating and chemical analysis.

4.1.2. Kone

We dated ignimbrite samples MER132A (Fontijn et al., 2018) from the Qpk eruption of Kone described by Rampey et al. (2010) and MER140B (Table 1), which have similar glass major element compositions and are attributed to the same eruption (Fontijn et al., 2018; Iddon et al., 2019). We also dated sample MER141A, which is from a pumice fall deposit with a chemical composition distinct from that of the Qpk deposits (Fontijn et al., 2018). The stratigraphic relationship between MER141A and Qpk (MER132A/MER140B) is undetermined.

4.1.3. Gedemsa

We dated samples MER080B, MER084A and MER077B (Table 1) associated with the caldera formation (Fontijn et al., 2018), and analysed their trace element composition.

4.1.4. Shala

In 2017, we sampled proximal units of the Quaternary Shala eruptive sequence exposed around the lake. We dated and analysed ignimbrites Qi4a (sample E76/50), and Qi5 (sample E76/61) of Mohr et al. (1980), as well as pumices from Qr2a (ETH17-1QR2A), sampled above an apparent erosional contact with the Qi5 ignimbrite at site ETH17-1 (Figs. 1b and 2c).

At site ETH17-15, ~10 km E of Lake Shala (Fig. 1b), we sampled a light beige, coarse ash-sized tephra (ETH17-15 F, Table 1), 2 m above a sequence of accretionary lapilli deposits attributed to pyroclastic density currents (PDCs, Fig. 2f). At site ETH17-17, SW of lake Langano (Fig. 1b), we sampled pumice from an ignimbrite (samples ETH17-17C and ETH17-17D, Table 1), possibly related to Shala's youngest caldera formation (Fig. 2g).

4.2. Distal samples from tephra archives

Fig. 3 depicts a schematic framework of distal sedimentary formations from which far-travelled (presumed-) MER tephra has been described (Brown and Fuller, 2008; Clark et al., 2003; Ian McDougall et al., 2005; Morgan and Renne, 2008) and from which tephra samples were collected for this study. Here, we report previously published $^{40}Ar/^{39}Ar$ ages of known tephra horizons recalculated with the new ^{4}K decay constants of Renne et al. (2011). All ages presented are reported as weighted mean $\pm$ 2 s. e.m (2σ).

4.2.1. Gademotta-Kulkuletti formation

The Gademotta and Kulkuletti sites are located west of Lake Ziway in the MER (Fig. 1b), east of the Gademotta ridge. The formation includes three tephra layers (Laury and Albritton, 1975; Morgan and Renne, 2008), from lowest to uppermost: Unit 10 (283 $\pm$ 3 ka), unit D (191 $\pm$ 4 ka) and unit 15 (Fig. 3d). Previous attempts to date unit 15 were unsuccessful due to crystal contamination (Morgan and Renne, 2008) but, based on
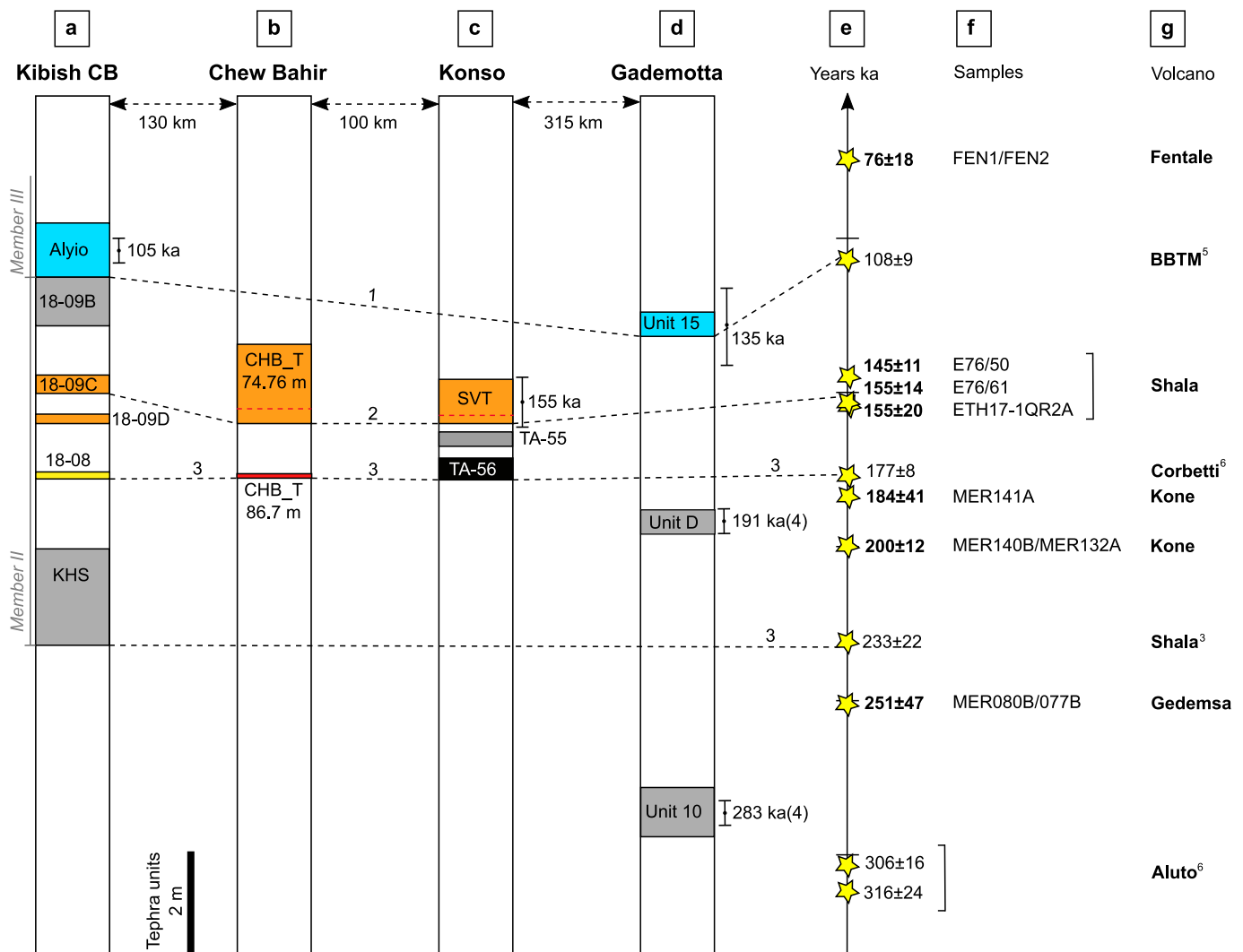

Fig. 3. a–d Schematic logs (not to scale) of distal tephra archives (see locations on Fig. 1) of the Main Ethiopian Rift with **e** dated MER ignimbrites (data at 2σ) and **f** samples analysed in this work from middle and late Pleistocene eruptions of **g** MER calderas whose associated ignimbrites have been dated, both previously and in the present study, together with their ages. The ages obtained in the present study are shown in bold. Tephra unit colours in **a–d** correspond with those displayed in Fig. 5. Grey units are not discussed in this work. Tephra unit thicknesses are to scale. Ages and 2σ uncertainties (error bars) are reported next to tephra units. Numbers on dashed lines indicate previously established correlations, after: 1. Brown et al. (2012), 2. Roberts et al. (2021) and 3. Vidal et al. (2022). Previous dating indicated as: 4. Morgan and Renne (2008), 5. Tadesse et al. (2022) and 6. Hutchison et al. (2016a). New tephrostratigraphic correlations are discussed in Section 6.

geochemical evidence, Brown et al. (2012) correlated it with the Aliyo Tuff in Omo-Kibish (see next section, Fig. 3), which has an age of 105 ± 5 ka (McDougall et al., 2005). We sampled and reanalysed the tephrochemistry of these three units (Fig. 3d, Table 1).

4.2.2. Omo-Kibish formation members II and III

The Omo-Kibish Formation is located north of lake Turkana, close to the Kenya/Ethiopia border (Fig. 1a), where fossils of Homo sapiens Omo I were found (see Fleagle et al., 2008 for a review). The formation bears many tephra layers in its members I to IV, the dating of which has been crucial for constraining ages of the hominin fossils (Vidal et al., 2022; Brown et al., 2012; Brown and Fuller, 2008; McDougall et al., 2005; Millard, 2008). Member II of the formation includes the KHS tuff (Brown and Fuller, 2008), recently correlated with an eruption of Shala at ca. 233 ± 22 ka (Vidal et al., 2022), and now defining a minimum age of the Omo I *H. sapiens,* found in underlying Member I (Fig. 3a). Vidal et al. (2022) also identified a tuff above KHS at Chibele South (CS), which they correlated with the ca. 177 ka Corbetti eruption (Fig. 3).

We traced this deposit in the field from the CS section to the Chibele (CB) type section of Brown and Fuller (2008), revisiting the site (Fig. 4) where Brown and Fuller (2008) described four tuffs, from bottom to top: KHS, CRF-23, and CRF-25 in member II, and the Aliyo tuff in member III (Fig. 4b).

Above the ca. 177 ka Corbetti tuff (ETH18-08), which might stratigraphically correspond with the CRF-23 deposit of Brown and Fuller (2008), we identified four tephra deposits (Fig. 4b). At the base of section, there is a ~20 cm thick, grey, crystal-rich fine-sand grade tephra layer (ETH18-09D, Fig. 4c). About 1 m above ETH18-09D lies a 10−50-cm-thick, white, fine silt grade, strongly laminated tuff (ETH18-09C, Fig. 4c). At the top of the sequence, two tuffs are superposed, ETH18-09 B and ETH18-09 A, which correspond to CRF-25 and the Aliyo Tuff, respectively (Fig. 4). The >100-cm-thick ETH18-9B deposit represents the top of Member II at this site, and is disconformable with the overlying >110-cm-thick Aliyo Tuff (sample ETH18-09A) which represents the base of Member III (Fig. 4). Laminations in the latter deposit are suggestive of reworking. The Aliyo Tuff was dated at 105 ± 5 ka (McDougall et al.,

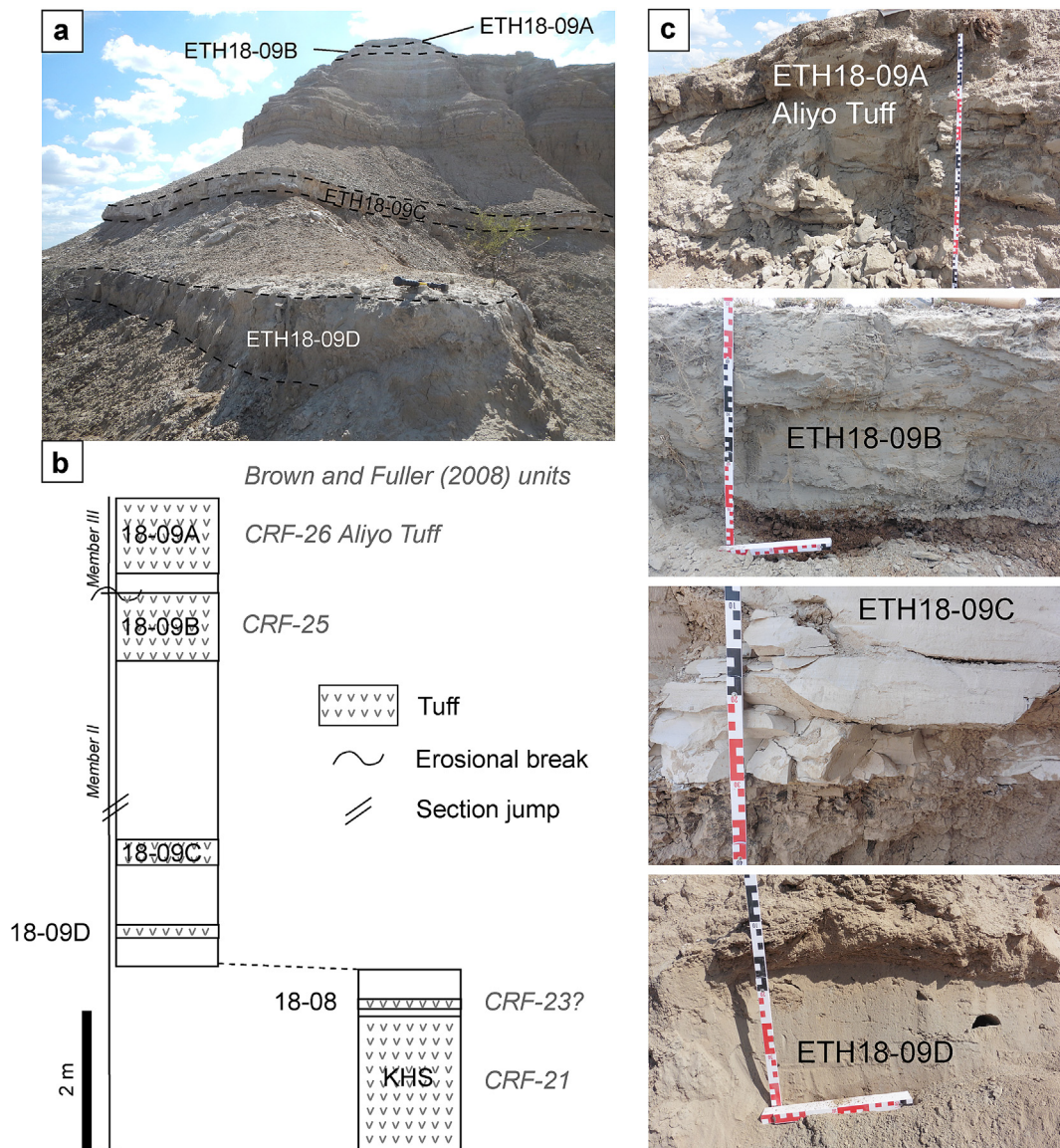**Fig. 4.** **a** Chibele site at Kibish. **b** Revised synthetic stratigraphy of the Chibele section showing correlation with units (grey italics) of Brown and Fuller (2008). **c** Photographs of the tuffs at Chibele.

2005) and geochemically linked to Gademotta Unit 15 (Fig. 3d, Brown et al., 2012) based on published major element compositions of the latter (Morgan and Renne, 2008). We also sampled the Aliyo Tuff (sample ETH18-02) at the CS type locality (Fig. 1a).

4.2.3. Chew Bahir sediment core

The Chew Bahir palaeolake is located within the Weyto-Chew Bahir tectonic basin in the southern Ethiopian Rift (Fig. 1a). Its sediments were recovered by the Chew Bahir Drilling Project (CBDP) whose main aim was to investigate linkages between climate change and hominin evolution in Africa (Foerster et al., 2012, 2018; Trauth et al., 2018, 2019; Viehberg et al., 2018). The 293-m-long (composite length) Chew Bahir core recovered in 2014 provides insights into the past 620 ka of the region's environmental history (Foerster et al., 2012; Trauth, 2021; Roberts et al., 2021), a timespan that includes the transition to the Middle Stone Age, and the origin and dispersal of *Homo sapiens*. Roberts et al. (2021) identified and analysed a visible tephra horizon in the Chew Bahir core (CHB_T74.755) at a basal composite depthof 74.755 mcd (mean composite depth) which they correlated with the 155 ± 14 ka Silver Tuff (SVT) in the Konso formation (Fig. 3; Clark et al., 2003; Katoh et al., 2000; Nagaoka et al., 2005). We sampled potential (crypto)tephra-bearing zones from core segments dating to between ~190 and 130 ka for cryptotephra counting and analysis.

5. ^{40}Ar/^{39}Ar ages and glass geochemistry

We obtained ages of six eruptions from four eruptive centres (Table 1). In this section, we report salient information for each eruptive unit, from oldest to youngest. We associate the voluminous MER ignimbrites to caldera-forming events, though acknowledge the need for much more detailed 'physical volcanology' fieldwork in the region. We calculated volumes of silicic magma associated with caldera formation not previously reported in the literature based on caldera dimensions and morphology following the method of Hutchison et al. (2016a). Averaged analyses (Table 2) and scatter plots of proximal samples (Fig. 5) provide geochemical fingerprints of the Middle and Late Pleistocene MER ignimbrites, and provide the basis for identifying the source of unknown medial and distal tephra horizons through classification (section 6.1). The analysed samples display similar incompatible trace element abundances (Table 2) and trends, precluding straightforward differentiation on biplots. This compositional similarity likely points to commonalities of the mantle source and storage and fractionation paths of the magmas feeding each volcano. We resort accordingly to trace element ratios (Fig. 5) to accentuate minor compositional differences and remove the potential effect of intensity variations. Fig. 5 reveals some overlap in trace element ratios representing neighbouring volcanoes, e.g. BBTM and Gedemsa.

5.1. Gedemsa ca. 251 ka

^{40}Ar/^{39}Ar dating of samples MER080B and MER077B of the same ignimbrite yield a mean composite age of 251 ± 47 ka (Table 1 and Fig. S1), consistent with the age range ca. 265–319 ka suggested by Peccerillo et al. (2003). Glasses from MER084A (equivalent to MER080B, Fontijn et al., 2018) have a homogeneous pantelleritic rhyolite composition (Fontijn et al., 2018), similar to other deposits from central MER volcanoes including BBTM, Shala and Corbetti (Fig. 5). Trace element ratios in MER084A overlap those of the ca. 108 ka BBTM (Meki) ignimbrite but are distinguished by higher Th content (Fig. 5).

5.2. Kone ca. 184 and ca. 200 ka

We estimate a total erupted volume of 6–14 km³ DRE associated with the caldera formation of Kone (Supplementary Table S5). Samples MER132A and MER140B (Fontijn et al., 2018) date to 199 ± 17 ka and 200 ± 16 ka, respectively (Table 1 and Fig. S2). MER139A (equivalent to MER140B, Table 1) shows evidence of alkali exchange, but otherwise these two samples have a similar comenditic to pantelleritic composition (Table 2, Fig. 5). The very close age of the samples further suggests they represent the same eruption Qpk, yielding a composite age of 200 ± 12 ka (Table 1, Fig. S2). Sample MER141A is dated 184 ± 42 ka (Table 1 and Fig. S3) and has a pantelleritic rhyolite composition (Fontijn et al., 2018) (Table 2, Fig. 5) distinct from that of the Qpk products, suggesting it represents a different eruption of the KVC. Trace element analyses were only conducted on MER132A, which stands out from other MER ignimbrites owing to lower La/Th and higher Zr/Y values (Fig. 5).

5.3. Shala ca. 155–145 ka

The green welded ignimbrite Qi4a dates to 145 ± 11 ka (Table 1 and Fig. S4), and the overlying coarse, matrix-poor and lithic-rich Qi5 ignimbrite yielded an age of 155 ± 14 ka (Table 1 and Fig. S4). The Qi4a pantellerite is geochemically less evolved than the Qi5 ignimbrite (Table 2, Fig. 6a). Qr2a yielded an age of 155 ± 20 ka (Table 2 and S1; Fig. S4), which statistically overlaps the ages of the underlying ignimbrites Qi4a and Qi5. Qr2a shares a similar composition with Qi5 (Table 2, Fig. 6a), which, together with the overlapping ages, suggests that Qi4a, Qi5 and Qr2a represent different phases of the same caldera-forming eruption at ca. 145–155 ka. Major element abundances of pumice ETH17-17C/D overlap the compositional range of Qr2a (Fig. 6a), while those of the ETH17-15 F overlap the intermediate and more evolved signature of the ca. 145–155 ka deposits (Fig. 6a). Trace element signatures (Fig. 6a) confirm that samples ETH17-17C/D and ETH17-15 F originate from the ca. 145–155 ka Shala eruption.

5.4. Fentale ca. 76 ka

The size of Fentale caldera suggests an eruptive volume of 6–7 km³ DRE (Supplementary Table S5). ^{40}Ar/^{39}Ar dating of samples FEN1 and FEN2 of the ignimbrite yield a mean composite age of 76 ± 18 ka (Table 1 and Fig. S6). Glassy enclaves in the devitrified matrix of ignimbrite sample FEN1 have a pantelleritic rhyolite composition (69–73 wt% SiO_2; 8.5 ± 0.6 wt% Al_2O_3; 8.3 ± 0.3 wt% FeO*; 10.2–11.2 wt% $Na_2O + K_2O$, Table 2) and display the highest FeO* abundances amongst the MER products analysed (Fig. 5). Trace element compositions of FEN1 glass (Fig. 5) also show distinctively low Zr/Y values compared with other MER centres, while Zr/Rb and La/Th ratios overlap those of Shala (Fig. 5).

5.5. Distal tephra

5.5.1. Gademotta Unit 15

New ^{40}Ar/^{39}Ar dating of 67 sanidine grains of Unit 15 at Gademotta provided an age of 135 ± 20 ka (Table 1 and Fig. S7). This is comparable (but not overlapping at 2σ) with the reported age of 105 ± 5 ka for the Aliyo Tuff in Member I of the Kibish Formation (McDougall et al., 2005), and geochemically correlated to Unit 15 by Brown et al. (2012).

5.5.2. Chew Bahir cryptotephra units CHB_T86.70

Core sections CHB−2B-49-1 and CHB−2B-48-1 comprise disturbed alluvial silt, silty sand and laminated muds, most likely

Table 2
Average major, minor and trace element composition of samples studied.

	Fentale		Kone		Gedemsa		Shala		Shala		Shala		Shala		Shala	
Volcano/formation																
Unit	Caldera		Caldera		Caldera		caldera QR2A		caldera Qi4		caldera Qi5		caldera?		caldera?	
Sample ID	FEN1		MER132A (2)		MER077B/084A (2)		ETH17-1QR2A		E76/50		ETH76/61		ETH17−17C,D		ETH17−15F	
Rock type	Welded Ignimbrite		Pumice (ignimbrite)		Pumice (ignimbrite)		Pumice (fallout)		Welded Ignimbrite		Pumice (ignimbrite)		Pumice (fallout)		Pumice (fallout)	
Age (ka) ± 2s w/J	**65 ± 17 (1)**		**199 ± 16**		**285 ± 110**		**155 ± 20**		**155 ± 11**		**149 ± 14**					
Wt%	*Avg (n = 24)*	*SD*	*Avg (n = 23)*	*SD*	*Avg (n = 43)*	*SD*	*Avg (n = 25)*	*SD*	*Avg (n = 25)*	*SD*	*Avg (n = 16)*	*SD*	*Avg (n = 16)*	*SD*	*Avg (n = 24)*	*SD*
SiO_2	71.6	1.1	75.90	0.24	74.60	0.47	74.67	0.33	74.08	0.70	74.83	0.35	74.80	0.40	74.70	0.33
TiO_2	0.40	0.08	0.21	0.04	0.28	0.04	0.34	0.02	0.29	0.03	0.33	0.03	0.34	0.02	0.35	0.01
Al_2O_3	8.46	0.55	9.74	0.15	9.18	0.24	9.91	0.36	8.42	0.20	9.57	0.37	9.83	0.35	9.57	0.26
FeO*	8.27	0.26	3.73	0.19	5.51	0.18	4.89	0.41	6.35	0.56	4.82	0.56	5.01	0.50	5.39	0.35
MnO	0.36	0.04	0.12	0.05	0.20	0.04	0.28	0.08	0.31	0.07	0.26	0.04	0.27	0.07	0.29	0.06
MgO	0.02	0.00	0.02	0.02	0.01	0.01	0.02	0.01	0.02	0.03	0.01	0.00	0.02	0.02	0.02	0.01
CaO	0.42	0.08	0.17	0.03	0.22	0.02	0.25	0.03	0.21	0.09	0.23	0.02	0.26	0.02	0.24	0.03
Na_2O	5.69	0.29	5.43	0.21	4.99	0.97	4.76	0.20	5.72	0.39	5.13	0.15	4.52	0.51	4.52	0.21
K_2O	4.80	0.32	4.68	0.15	5.00	0.66	4.86	0.18	4.48	0.36	4.79	0.13	4.93	0.37	4.91	0.40
P_2O_5	0.03	0.02	0.01	0.01	0.01	0.01	0.01	0.01	0.01	0.01	0.01	0.01	0.02	0.01	0.01	0.01
Cl	n.a	n.a	n.a	n.a	0.1818	0.0221	0.1772	0.0372	0.1094	0.0687	0.1574	0.0240	0.1590	0.0107	0.1773	0.0206
$Na_2O + K_2O$	10.49	0.29	10.10	0.24	9.99	0.50	9.63	0.23	10.20	0.18	9.93	0.11	9.45	0.29	9.43	0.31
ppm	*n = 16*		*n = 15*		*n = 23*		*n = 7*						*n = 20*		*n = 8*	
Rb	198	123	258.2	25.1	142.0	18.1	169	76					157	77	105	10
Sr	9.9	1.4	1.8	0.3	1.5	0.6	6.2	6.6					24.4	37.6	1.3	0.8
Y	135	32	155.9	15.0	102.8	11.2	167	76					150	61	100	7
Zr	1029	281	1623.9	118.7	930.4	98.9	1500	704					1336	528	918	71
Nb	189	46	276.2	21.3	145.1	14.0	240	109					210	83	148	14
Cs	2.4	3.0	3.7	0.7	1.7	0.4	1.5	0.7					1.5	0.8	0.9	0.1
Ba	571	66	17.1	1.9	31.3	4.1	30	14					28	15	16	3
La	129	30	150.5	10.5	111.2	12.0	198	90					177	71	120	10
Ce	263	56	319.4	33.9	232.6	23.7	411	186					392	162	264	29
Pr	30	7	32.5	2.9	25.2	2.7	46	21					42	17	29	2
Nd	125	27	124.0	12.3	101.7	11.6	182	81					163	62	114	10
Sm	26	6	24.7	2.9	20.1	2.6	37	16					33	14	22	2
Eu	6.2	1.1	2.1	0.2	2.7	0.3	4.2	2.0					4.0	1.6	2.7	0.4
Gd	25	5	23.8	2.2	18.5	2.4	32	16					29	12	20	2
Dy	26	6	27.9	2.5	19.7	2.2	32	15					29	12	20	2
Er	15	4	17.7	1.8	11.5	1.4	18	8					16	7	11	1
Yb	15	4	18.8	1.8	11.0	1.0	17	8					15	7	10	1
Hf	25	7	38.4	3.7	23.3	2.1	35	16					32	13	21	2
Ta	11.5	2.9	17.7	1.7	9.0	0.6	14.5	6.6					13.6	5.4	9.0	0.9
Pb	19	4	32.0	4.6	26.3	2.9	23	11					22	14	16	2
Th	18	4	32.8	3.1	19.0	1.7	25	11					23	9	16	1
U	4.9	1.3	8.9	1.1	4.8	0.5	6.7	3.1					6.4	2.7	4.4	0.6
La/Th	7.4	0.3	4.6	0.2	5.8	0.3	8.0	0.2					7.7	0.7	7.6	0.2
Nb/Th	10.8	0.5	8.5	0.6	7.6	0.5	9.7	0.7					9.2	1.3	9.4	0.4
Zr/Rb	6.3	2.3	6.3	0.5	6.6	0.6	8.9	0.7					8.8	0.8	8.8	0.4
Zr/Y	7.6	0.4	10.4	0.4	9.1	0.4	8.9	0.3					9.2	1.8	9.2	0.3
Ce/Pb	13.7	2.0	10.1	1.2	9.8	1.1	18.3	1.9					19.0	5.4	16.6	0.5

n: number of analyses; Avg: average; SD: standard deviation; FeO*: FeO total.
(1) composite age of FEN1 and FEN2.
(2) Major element from Fontijn et al. (2018).
(2) McDougall et al. (2005)
(3) Ages from Morgan and Renne (2008), major and trace data for Unit D are from Vidal et al. (2022).
(4) Clark et al. (2003), recalculated by Roberts et al. (under review).
(5) Major element abundances from Roberts et al. (2021), trace abundances from this study.

| Gademotta		Gademotta		Gademotta		Kibish		Kibish		Kibish		Kibish		Chew Bahir		Chew Bahir		Konso	
Unit 15		Unit D		Unit 10		Alyio		Alyio		SVT		SVT		CHB_T74.755		CHB_T86.70		SVT	
ETH17−19 Ash		ETH17−20		GAD10		ETH18−2 Tuff		ETH18-9A Tuff		ETH18-9C Tuff		ETH18-9D Ash		OcT 9984/10663/10662		CT648 Cryptotephra		ETH18−14F	
126 ± 19		**191 ± 4 (3)**		**302 ± 6 (3)**		**105 ± 5 (3)**								**155 ± 14 (5)**		**177 ± 10**		**155 ± 14 (4)**	
Avg (n = 36)	SD	*Avg (n = 88)*	SD	*Avg (n = 33)*	SD	*Avg (n = 24)*	SD	*Avg (n = 30)*	SD	*Avg (n = 30)*	SD	*Avg (n = 22)*	SD	*Avg (n = 63)*	SD	*Avg (n = 31)*	SD	*Avg (n = 27)*	SD
75.93	0.73	75.74	0.63	75.77	0.35	76.29	0.44	76.11	0.41	77.02	0.60	76.44	0.54	74.23	0.82	75.12	0.37	76.23	0.53
0.35	0.01	0.34	0.03	0.29	0.02	0.36	0.01	0.35	0.01	0.34	0.02	0.35	0.03	0.33	0.04	0.34	0.01	0.35	0.03
9.11	0.16	9.90	0.24	9.36	0.15	9.07	0.10	9.08	0.13	9.63	0.45	9.64	0.49	9.44	0.64	9.34	0.30	9.41	0.55
6.37	0.17	5.68	0.21	6.20	0.30	6.40	0.16	6.38	0.14	5.46	0.58	5.45	0.62	5.48	0.56	5.36	0.42	5.78	0.62
0.28	0.05	0.24	0.04	0.28	0.04	0.27	0.03	0.27	0.04	0.30	0.05	0.28	0.06	0.24	0.07	0.31	0.05	0.31	0.05
0.01	0.00	0.01	0.01	0.02	0.01	0.01	0.01	0.01	0.01	0.01	0.01	0.01	0.01	0.01	0.02	0.03	0.01	0.02	0.01
0.25	0.02	0.27	0.02	0.26	0.02	0.27	0.02	0.26	0.03	0.24	0.02	0.25	0.02	0.25	0.06	0.22	0.02	0.25	0.02
3.10	0.89	3.14	0.69	3.16	0.32	2.77	0.28	2.86	0.29	2.50	0.46	2.93	0.47	5.55	0.37	4.85	0.17	2.88	0.47
4.58	0.11	4.66	0.26	4.65	0.30	4.41	0.13	4.44	0.11	4.49	0.25	4.50	0.27	4.28	0.32	4.43	0.22	4.56	0.13
0.02	0.02	0.02	0.02	0.01	0.01	0.01	0.01	0.02	0.02	n.a	n.a	0.02	0.02	0.01	0.02	0.01	0.02	0.02	0.01
0.2266	0.0016	0.1581	0.0356	n.a	n.a	0.2124	0.0140	n.a	n.a	0.1604	0.0345	n.a	n.a	0.1762	0.0351	n.a	n.a	0.2084	0.0432
7.68	0.87	7.80	0.65	7.81	0.24	7.19	0.39	7.30	0.36	6.99	0.68	7.43	0.69	9.83	0.48	9.28	0.35	7.44	0.47
n = 22		n = 36		n = 16		n = 11								n = 35		n = 18		n = 18	
133	3	119	10	189	16	163	10							113	22	121	13	137	24
1.6	0.5	2.2	2.1	7.3	9.9	1.7	0.3							0.8	0.2	1.5	0.3	1.1	0.5
108	3	93	10	151	15	124	7							121	32	126	19	152	41
986	41	854	88	1433	128	1125	42							1085	278	1167	173	1378	335
150	3	120	8	283	19	195	15							166	42	193	19	223	48
1.5	0.3	1.2	0.1	1.8	0.4	1.9	0.2							1.0	0.3	1.3	0.2	1.2	0.3
20	1	119	184	102	22	23	2							14	3	35	8	16	3
120	5	102	6	188	13	136	6							140	36	131	19	172	43
251	8	212	14	382	36	302	23							292	75	298	37	380	86
28	1	24	2	41	3	32	1							33	8	33	5	40	10
110	4	94	8	163	14	128	4							132	33	128	19	167	40
22	1	19	2	31	3	27	1							26	6	26	4	34	9
2.7	0.1	2.7	0.8	4.7	0.5	3.1	0.1							3.1	0.9	3.8	0.4	4.0	1.1
20	1	17	2	28	3	23	1							23	6	23	4	29	8
21	1	18	2	28	3	24	2							23	6	25	4	28	7
12	0	10	1	17	2	14	1							13	3	14	2	17	4
12	0	10	1	17	3	13	1							12	3	14	2	16	4
24	1	21	2	35	4	28	1							26	7	26	4	32	8
9.4	0.4	7.3	0.5	17.4	1.4	11.3	0.3							10.3	2.6	10.9	1.4	13.9	3.0
21	1	19	2	30	3	30	3							18	6	19	3	23	5
18	1	16	1	30	3	22	1							18	5	15	2	25	7
4.6	0.2	3.9	0.3	7.6	1.0	6.1	0.7							5.0	1.3	4.6	0.6	6.5	1.4
6.5	0.2	6.3	0.4	6.2	0.4	6.2	0.2							7.7	0.5	8.9	0.4	7.0	0.5
8.1	0.4	7.5	0.7	9.4	0.8	8.9	0.6							9.2	0.6	13.3	1.9	9.3	1.3
7.4	0.2	7.3	1.2	7.6	0.9	6.9	0.5							9.5	0.7	9.7	1.0	10.1	2.0
9.1	0.1	9.2	0.3	9.5	0.4	9.1	0.4							9.0	0.3	9.3	0.3	9.2	0.4
11.8	0.5	11.3	1.7	13.0	0.9	10.1	0.7							16.9	1.8	15.4	0.9	16.4	1.6
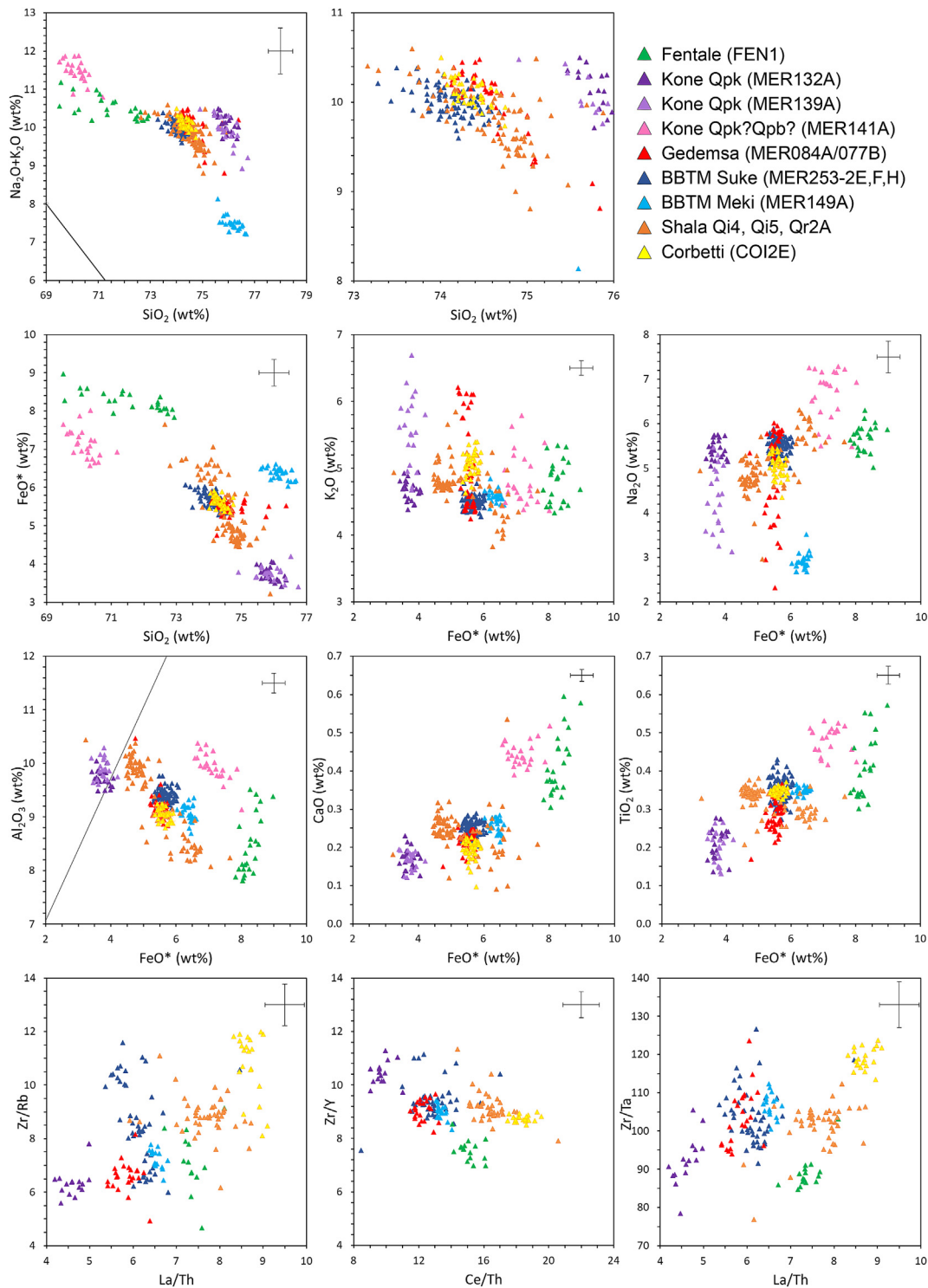
Fig. 5. Major and trace element compositions of glasses from proximal MER ignimbrite samples. Where stratigraphic unit names are not available, our sample references are reported. Major and trace data for the BBTM Meki and Suke eruptions are from Tadesse et al. (2022). Major element data for Kone and Gedemsa samples are from Fontijn et al. (2018). Analyses for the three units of the 155−145 ka Shala eruption are combined for clarity (see Fig. 3 for split compositions). Major element data are normalized to 100% anhydrous (see average compositions in Table 2, dataset in Supplementary Table S3). Error bars shown are relative standard deviations derived from repeat measurements of matrix match glass secondary standards STH-S6 (for FeO*, $n = 151$; Supplementary Table S2) and ATHO-G (for Al_2O_3, CaO and TiO_2, $n = 107$; Supplementary Table S2). They are plotted in the top right corner of each plot for clarity and rescaled to the value of the centre point. In the case of element ratios, error propagation has been applied using analyses of standard ATHO-G ($n = 13$; Supplementary Table S4).
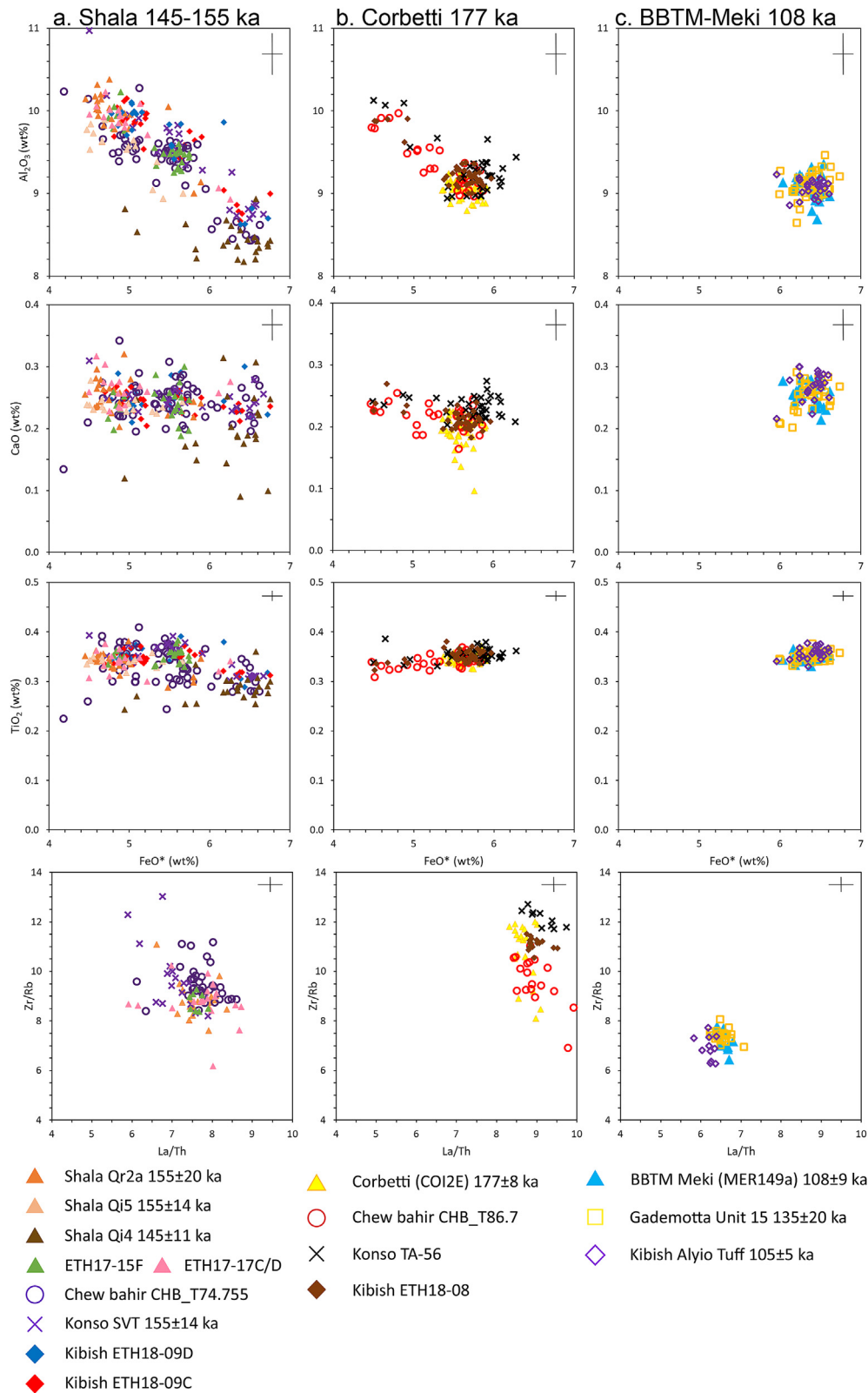
Fig. 6. Geochemical correlations of selected MER ignimbrites with distal correlatives (see average compositions in Table 2) for **a** the ca. 145−155 ka Shala eruption, **b** the ca. 177 ka Corbetti eruption, and **c** the ca. 108 ka BBTM eruption (Tadesse et al., 2022). Major element composition of Konso TA-55 tuff from Vidal et al. (2022) and Konso SVT and CHB_T74.755 from (Roberts et al., 2021). Major element data are normalized to 100% anhydrous (see average compositions in Table 2, dataset in Supplementary Table S3). Error bars shown are relative standard deviations derived from repeat measurements of matrix match glass secondary standards STH-S6 (for FeO*, $n = 151$; Supplementary Table S2) and ATHO-G (for Al$_2$O$_3$, CaO and TiO$_2$, $n = 107$; Supplementary Table S2). They are plotted in the top right corner of each plot for clarity and rescaled to the value of the centre point. In the case of element ratios, error propagation has been applied using analyses of standard ATHO-G ($n = 13$; Supplementary Table S4).

fragmented during drilling. There is visible evidence of upward injection of drilling fluids and entrained fines alongside the edge of the core liner. Cryptotephra analyses from sections CHB−2B-49-1 and CHB−2B-48-1 reveal the presence of volcanic glass shards throughout these two core sections, spanning 86.70−85.96 m mean composite depth. Glass shards are transparent with curvilinear forms. The highest glass shard concentrations (≫10,000 shards per g of dry sediment) and the largest glass shard sizes (<120 μm along the longest axis) occur between 86.55 and 86.45 m, locating the most likely position of the primary deposit. The age model of the Chew Bahir core (Roberts et al., 2021) indicates an age of 178 ± 11 ka for this cryptotephra-rich horizon. Glass shard concentration and size decreases gradually above this interval. Shards in CHB_T86.70 have pantelleritic peralkaline rhyolite compositions with normalised values of 75.1 ± 0.6 wt% SiO_2, 9.3 ± 0.6 wt% Al_2O_3, 5.3 ± 0.8 wt% FeO*, 4.9 ± 0.3 wt% Na_2O and 4.5 ± 0.3 wt% K_2O (Table 2).

5.5.3. Kibish units ETH8-9D and ETH18-9C

Samples ETH18-9D and ETH18-9C have identical pantelleritic compositions, with 76.4−77 wt% SiO_2, 9.6 ± 0.5 wt% Al_2O_3, 5.5 ± 0.6 wt% FeO*, and 4.5 ± 0.3 wt% K_2O (Table 2). Na_2O contents are slightly lower in ETH18-9C (2.5 ± 0.5 wt%) than in ETH18-9D (2.9 ± 0.5 wt%).

6. Geochemical correlations of proximal and distal tephra

All the MER eruptions we have characterised will have generated major ash plumes likely to provide valuable chronostratigraphic control for diverse sedimentary archives. Here we discuss correlations of three major eruptions with tephra from the Gademotta-Kulkuletti, Konso and Omo-Kibish formations and from the Chew Bahir sediment core. We note that several distal tephra horizons are yet to be associated with proximal deposits, possibly from smaller magnitude events or other large eruptions yet to be identified. Similarly, distal deposits of Fentale, KVC and Gedemsa ignimbrites are yet to be recognised.

6.1. Distal correlatives of the ca. 155−145 ka Shala eruption

The range of major element compositions of the Shala caldera units (Qi4a, Qi5, and Qr2a) systematically overlaps those of the 155 ± 14 ka SVT (sample ETH18-14 F) from the Konso Formation (Clark et al., 2003; Katoh et al., 2000) and CHB_T74.55 (Roberts et al., 2021) (Fig. 6a). The SVT age of 155 ± 14 ka is consistent with our new ages of the Shala caldera units, i.e., ca. 155 ka (Qr2a), ca. 155 ka (Qi5), and ca. 145 (Qi4) (Table 1). These correlations are supported by the overlap of trace element ratios in the Shala samples, the SVT and the CHB_T74.755 tephra (Fig. 6a).

Fig. 6a further shows that Kibish tuffs ETH18-9C and ETH18-9D from the CB section (Fig. 6) are compositionally similar to the SVT and proximal Shala products. Given that the two tuffs ETH18-9C and ETH18-9D are separated by ca. 1 m of weathered lacustrine sediment, likely to represent an interval of order 2 ka based on average sedimentation rates at Chew Bahir of ca. 47 cm/ka (Roberts et al., 2021), this indicates two separate eruptions of very similar magmas. Intermittent eruptive pulses within a few thousand years at Shala might be differentiated in the proximal stratigraphy, but cannot be resolved from the available geochronology (Table 1). We hypothesise that the uppermost of the two tuffs, ETH18-9C, corresponds to the 155 ka SVT at Konso. The lower tuff ETH18-9D might be the equivalent of the Konso tuff TA-55, however the sample that we collected from the latter was unsuitable for analysis due to severe weathering and devitrification (Vidal et al., 2022). Tuff TA-55 occurs between SVT and TA-56 (Fig. 3), which is

correlated with the ca. 177 ka Corbetti eruption (Vidal et al., 2022). An age of ca. 155 ka for ETH18-9C is consistent with its stratigraphic position below the ca. 105 ka Alyio Tuff at the Kibish CB section.

The wide compositional range of the proximal units of the ca. 145−155 ka Shala eruption is entirely reflected in all distal samples (Fig. 6a). The revised stratigraphy at Kibish (Fig. 3) indicates that Shala is the source of two widespread tuffs deposited between 177 ka and 155 ka (Fig. 4). The ca. 155 Shala tephra is found in Konso (SVT), ~260 km SSW of the caldera (Fig. 1), where it is ~90 cm-thick. The top ~75 cm of the SVT outcrop sampled by Vidal et al. (2022) is pedogenically altered, grading into a paleosol, hindering estimation of the unit's original thickness, but beneath this is preserved ~15 cm of pristine ash. About 370 km SSW and SW of Shala, the deposit is ~20 cm thick at Kibish, and the visible ash in the Chew Bahir core spans 14.5 cm (Roberts et al., 2021). This eruption therefore constitutes a key chronostratigraphic marker (Fig. 3) for palaeoclimatic and palaeoanthropological records in southern Ethiopia, and likely extends into Northern Kenya, including in the Turkana basin.

6.2. Distal correlatives of the ca. 177 ka Corbetti eruption

Fig. 6b shows that major and trace element abundances of the 178 ± 11 ka CHB_T86.70 glasses from the Chew Bahir core partially overlap those of the ca. 177 ka Corbetti ignimbrite (sample COI2E), and match well with the distal correlatives at Konso (TA-56) and Kibish (ETH18-8) (Vidal et al., 2022). CHB_T86.70 occurs ~12 m deeper in the Chew Bahir core stratigraphy than CHB_T74.755, which has been shown to be a correlative of the Konso SVT (155 ± 14 ka, Fig. 3; Roberts et al., 2021), providing the second stratigraphic tie-line between the Chew Bahir core and the Konso sequence (Fig. 3).

6.3. Distal correlatives of the ca. 108 ka BBTM eruption

New major element analyses of Gademotta Unit 15 and Kibish Alyio Tuff using the same analytical conditions (Fig. 6c) confirm the correlation first suggested by Brown et al. (2012). These two tephra are a close match with glasses from the ca. 108 ± 9 ka BBTM eruption (sample MER149A, Tadesse et al., 2022) from a caldera-forming event of the BBTM complex (Tadesse et al., 2022). These correlations are confirmed by overlap in trace element ratios (Fig. 6c). The age of 135 ± 20 ka we obtained for Unit 15 (Table 1) and those for the Kibish Alyio Tuff (105 ± 5 ka, McDougall et al., 2005) and BBTM eruption (108 ± 9 ka, Tadesse et al., 2022) are close enough that, given the use of different argon isotopic measurement protocols between studies (including the number of grains considered), we hypothesise that the ca. 108 ka BBTM eruption is the source of the ~50 cm-thick Gademotta Unit 15 and > 110 cm-thick Kibish Alyio tuff, respectively located ~50 km SW and ~460 km SW from BBTM (Figs. 1 and 3).

7. Revisiting the MER ignimbrite flare-up hypothesis

We have provided new age constraints for the caldera-forming eruptions at Fentale (ca. 76 ka), Shala (ca. 155−145 ka), Kone (ca. 184 ka and ca. 200 ka), and Gedemsa (ca. 251 ka) volcanoes. Adding the ca. 108 ka BBTM eruption (Tadesse et al., 2022), the ca. 177 ka Corbetti caldera (Hutchison et al., 2016b), the ca. 233 ka Shala eruption (possibly caldera-forming, Vidal et al., 2022), and the ca. 306−316 ka Aluto eruptions (Hutchison et al., 2016b), there is strong evidence for multiple large magnitude explosive eruptions in the MER during the middle-to-late Pleistocene, with the formation of up to nine calderas within ~230,000 years.

The new geochronological and tephrochronological aspects of this study refine and extend the existing record of middle to Late

Pleistocene explosive volcanism in the MER as shown in Fig. 3. There are additional calderas in the Afar Rift northeast of the MER that formed during the Middle Pleistocene including the ca. 295 ka Mallahle caldera and ca. 130 ka Nabro caldera (Oppenheimer et al., 2019). Notably, all these large-magnitude eruptions occurred within a timespan critical for understanding human speciation, dispersal and cultural innovation (Clark et al., 2003; Fleagle et al., 2008).

Both Mohr et al. (1980) and Hutchison et al. (2016a) considered that temporal clustering of colossal eruptions in the MER ca. 170−320 ka represents a silicic 'flare-up', invoking an increased mantle melt supply to axial volcano-tectonic segments of the MER and establishment of large magma reservoirs within structural traps (Hutchison et al., 2016b). Although the exposed stratigraphic record suggests hiatuses in activity at individual systems (e.g. Corbetti, Aluto; Hutchison et al., 2016b), overall, the new evidence presented here indicates continued ignimbrite eruptions until ca. 76 ka (that of Fentale; Fig. 3). Given that the regional eruption history (eruption ages and volumes) is still only partially revealed, designation of 'flare-ups' remains speculative. The Pleistocene and Pliocene stratigraphy in Ethiopia, studied extensively where human fossils and archaeological records have been sought, is replete with tephra horizons such as at Gona (Quade et al., 2008), Konso (Katoh et al., 2000) and Melka Wakena (Hovers et al., 2021; Resom et al., 2018). Few of these have been traced to their sources, some of which are likely geomorphologically and tectonically degraded, eroded and/or buried by younger volcanic products. Also, many known calderas have yet to be accurately dated, including Birenti (KVC), Boku (BVC), Gudda (BBVC) and Suke (BBTM) in the central MER, Wagebesa, Diguna and Hobicha in the southern sector of the MER, and Adoua, Ma'Alalta and Barra'Ale in Afar. Further systematic studies to trace and correlate proximal and distal deposits, and detailed geochronological, stratigraphic and sedimentological investigation of proximal records, are certainly called for.

8. Concluding remarks

We have reported ages and geochemical signatures of deposits from large-magnitude eruptions in the MER, some of them certainly caldera-forming, i.e., at Fentale (ca. 76 ka), Shala (ca. 145−155 ka), Kone (ca. 184 and 199 ka), and Gedemsa (ca. 251 ka) volcanoes. Geochronological comparisons and geochemical correlations of proximal and distal tephra deposits permitted to identify distal deposits of the ca. 108 ka BBTM, ca. 145−155 ka Shala, and ca. 177 ka Corbetti eruptions to sink in southern Ethiopia, notably in the Kibish and Konso Formations and the Lake Chew Bahir sedimentary record. As yet, distal deposits of Fentale, Kone and Gedemsa have not been recognised. The notable thickness of distal tephra in sedimentary depocenters several hundred kilometres from source suggests the units are likely represented in other sedimentary archives across eastern Africa and possibly offshore.

Using major, minor and trace element concentrations, measured using consistent analytical protocols, we have revised and extended previous correlations, improving the chronostratigraphic record of the central and southern MER. Our findings highlight the scope for future tephrochronological work in adjacent regions of northern Kenya and Afar, which can support dating of fossils and cultural layers in archaeological contexts. At least seven caldera-forming eruptions occurred between ca. 316 ka and ca. 76 ka, an interval critical for understanding the evolution and dispersal of *Homo sapiens* in and beyond eastern Africa. The revised chronology suggests a more prolonged middle and late Pleistocene episode of ignimbrite-forming eruptions in the MER than previously recognised, and emphasises the need for more work to evaluate the 'flare-up' hypothesis. More broadly, much deeper geochronological, stratigraphic and sedimentological studies are required to shed light on the magnitudes, styles and impacts of these prodigious eruptions.

Author contribution

Conceptualisation: CV, KF, CL, AA, WH, YM, CO. Formal analysis: CV, KF, CL, DB, ET, AP. Investigation: CV, KF, CL, AA, DB, ET, AP, WH, AT, GY, AD, YM, FW Conducting a research and investigation process, specifically performing the experiments, or data/evidence collection. Resources: PM, FW. Writing: CV, KF, CL, AA, DB, CO. Writing - Review & Editing: all authors. Visualisation: CV. Supervision: CV, KF, CL, AA, CO. Project administration: CV, KF, CL, AA, CO. Funding acquisition: KF, WH, CO, DP, TM.

Declaration of competing interest

The authors declare that they have no known competing financial interests or personal relationships that could have appeared to influence the work reported in this paper.

Acknowledgements

Appendix A. Supplementary data

Supplementary data to this article can be found online at https://doi.org/10.1016/j.quascirev.2022.107601.

References

Basell, L.S., 2008. Middle Stone Age (MSA) site distributions in eastern Africa and their relationship to Quaternary environmental change, refugia and the evolution of Homo sapiens. Quat. Sci. Rev. 27, 2484−2498. https://doi.org/10.1016/j.quascirev.2008.09.010.

Baumann, A., Förstner, U., Rohde, R., 1975. Lake Shala: water chemistry, mineralogy

and geochemistry of sediments in an Ethiopian Rift lake. Geol. Rundsch. 64, 593–609. https://doi.org/10.1007/BF01820685.

Biggs, J., Bastow, J.D., Keir, D., Lewi, E., 2011. Pulses of deformation reveal frequently recurring shallow magmatic activity beneath the Main Ethiopian Rift. Geochem. Geophys. Geosyst. 12. https://doi.org/10.1029/2011GC003662.

Bizouard, H., Paola, G.M., 1978. Mineralogy of the Tullu Moje active volcanic Area (Arussi: Ethiopian rift valley). Petrol. Geochem. Cont. Rift. 87–100. https://doi.org/10.1007/978-94-009-9803-2_9.

Blockley, S., Pyne-O'Donnell, S., QS, J.L., 2005. A new and less destructive laboratory procedure for the physical separation of distal glass tephra shards from sediments. Quat. Sci. Rev. 24, 1952–1960, 2005, U.

Boccaletti, M., Mazzuoli, R., Bonini, M., Trua, T., Abebe, B., 1999. Plio-Quaternary volcanotectonic activity in the northern sector of the Main Ethiopian Rift: relationships with oblique rifting. J. Afr. Earth Sci. 29, 679–698. https://doi.org/10.1016/S0899-5362(99)00124-4.

Brotzu, P., Morbidelli, L., Piccirillo, E.M., Traversa, G., 1974. Petrological features of boseti mountains, a complex volcanic system in the axial portion of the main Ethiopian rift. Bull. Volcanol. 38, 206–234. https://doi.org/10.1007/BF02597811.

Brown, F.H., Fuller, C.R., 2008. Stratigraphy and tephra of the Kibish formation, southwestern Ethiopia. J. Hum. Evol. 55, 366–403. https://doi.org/10.1016/j.jhevol.2008.05.009.

Brown, F.H., McDougall, I., Fleagle, J.G., 2012. Correlation of the KHS Tuff of the Kibish Formation to volcanic ash layers at other sites, and the age of early Homo sapiens (Omo I and Omo II). J. Hum. Evol. 63, 577–585. https://doi.org/10.1016/J.JHEVOL.2012.05.014.

Clark, J.D., Beyene, Y., WoldeGabriel, G., Hart, W.K., Renne, P.R., Gilbert, H., Defieur, A., Suwa, G., Katoh, S., Ludwig, K.R., Boisserie, J.R., Asfaw, B., White, T.D., 2003. Stratigraphic, chronological and behavioural contexts of Pleistocene Homo sapiens from middle Awash, Ethiopia. Nature 423, 747–752. https://doi.org/10.1038/nature01670.

Cole, J.W., 1969. Gariboldi volcanic complex, Ethiopia. Bull. Volcanol. 33, 566–578. https://doi.org/10.1007/BF02596525.

Corti, G., 2009. Continental rift evolution: from rift initiation to incipient break-up in the Main Ethiopian Rift, East Africa. Earth Sci. Rev. https://doi.org/10.1016/j.earscirev.2009.06.005.

Dakin, G, Gibson, I.L., 1971. A preliminary account of Alutu, a pantelleritic volcano in the Main Ethiopian Rift. Bull. Geophys. Obs. Addis Ababa 13, 110–114.

Di Paola, G.M., 1972. The Ethiopian Rift Valley (between 7° 00′ and 8° 40′ lat. north). Bull. Volcanol. 36, 517–560. https://doi.org/10.1007/BF02599823.

Fleagle, J., Assefa, Z., Brown, F., Evolution, J.S.-J. of human, 2008. Paleoanthropology of the Kibish formation, southern Ethiopia: introduction. Elsevier 55 (3), 360–365. U., 2008.

Foerster, V., Deocampo, D.M., Asrat, A., Günter, C., Junginger, A., Krämer, K.H., Stroncik, N.A., Trauth, M.H., 2018. Towards an understanding of climate proxy formation in the Chew Bahir basin, southern Ethiopian Rift. Palaeogeogr. Palaeoclimatol. Palaeoecol. 501, 111–123. https://doi.org/10.1016/J.PALAEO.2018.04.009.

Foerster, V., Junginger, A., Langkamp, O., Gebru, T., Asrat, A., Umer, M., Lamb, H.F., Wennrich, V., Rethemeyer, J., Nowaczyk, N., Trauth, M.H., Schaebitz, F., 2012. Climatic change recorded in the sediments of the Chew Bahir basin, southern Ethiopia, during the last 45,000 years. Quat. Int. 274, 25–37. https://doi.org/10.1016/J.QUAINT.2012.06.028.

Fontijn, K., McNamara, K., Zafu Tadesse, A., Pyle, D.M., Dessalegn, F., Hutchison, W., Mather, T.A., Yirgu, G., 2018. Contrasting styles of post-caldera volcanism along the Main Ethiopian Rift: implications for contemporary volcanic hazards. J. Volcanol. Geoth. Res. 356, 90–113. https://doi.org/10.1016/J.JVOLGEORES.2018.02.001.

Gibson, I.L., 1970. A pantelleritic welded ash-flow tuff from the Ethiopian Rift Valley. Contrib. Mineral. Petrol. 28, 89–111. https://doi.org/10.1007/BF00404992.

Hovers, E., Gossa, T., Asrat, A., Niespolo, E.M., Resom, A., Renne, P.R., Ekshtain, R., Herzlinger, G., Ketema, H., Martínez-Navarro, B., 2021. The expansion of the Acheulian to the Southeastern Ethiopian Highlands: insights from the new early Pleistocene site-complex of Melka Wakena. Quat. Sci. Rev. 253, 106763. https://doi.org/10.1016/J.QUASCIREV.2020.106763.

Hunt, J.A., Mather, T.A., Pyle, D.M., 2020. Morphological comparison of distributed volcanic fields in the Main Ethiopian Rift using high-resolution digital elevation models. J. Volcanol. Geoth. Res. 393, 106732. https://doi.org/10.1016/J.JVOLGEORES.2019.106732.

Hunt, J.A., Pyle, D.M., Mather, T.A., 2019. The geomorphology, structure, and lava flow dynamics of peralkaline rift volcanoes from high-resolution digital elevation models. Geochem. Geophys. Geosyst. 20, 1508–1538. https://doi.org/10.1029/2018GC008085.

Hutchison, W., Biggs, J., Mather, T.A., Pyle, D.M., Lewi, E., Yirgu, G., Caliro, S., Chiodini, G., Clor, L.E., Fischer, T.P., 2016a. Causes of unrest at silicic calderas in the East African Rift: new constraints from InSAR and soil-gas chemistry at Aluto volcano, Ethiopia. Geochem. Geophys. Geosyst. https://doi.org/10.1002/2016GC006395.

Hutchison, W., Fusillo, R., Pyle, D.M., Mather, T.A., Blundy, J.D., Biggs, J., Yirgu, G., Cohen, B.E., Brooker, R.A., Barfod, D.N., Calvert, A.T., 2016b. A pulse of mid-Pleistocene rift volcanism in Ethiopia at the dawn of modern humans. Nat. Commun. 7, 13192. https://doi.org/10.1038/ncomms13192.

Hutchison, W., Pyle, D.M., Mather, T.A., Yirgu, G., Biggs, J., Cohen, B.E., Barfod, D.N., Lewi, E., 2016c. The eruptive history and magmatic evolution of Aluto volcano: new insights into silicic peralkaline volcanism in the Ethiopian rift. J. Volcanol. Geoth. Res. https://doi.org/10.1016/j.jvolgeores.2016.09.010.

Iddon, F., Jackson, C., Hutchison, W., Fontijn, K., Pyle, D.M., Mather, T.A., Yirgu, G., Edmonds, M., 2019. Mixing and crystal Scavenging in the main Ethiopian rift revealed by trace element systematics in feldspars and glasses. Geochem. Geophys. Geosyst. 20, 230–259. https://doi.org/10.1029/2018GC007836.

Katoh, S., Nagaoka, S., WoldeGabriel, G., Renne, P., Snow, M.G., Beyene, Y., Suwa, G., 2000. Chronostratigraphy and correlation of the Plio-Pleistocene tephra layers of the Konso formation, southern main Ethiopian rift, Ethiopia. Quat. Sci. Rev. 19, 1305–1317. https://doi.org/10.1016/S0277-3791(99)00099-2.

Kuehn, S.C., Froese, D.G., Shane, P.A.R., 2011. The INTAV intercomparison of electron-beam microanalysis of glass by tephrochronology laboratories: results and recommendations. Quat. Int. https://doi.org/10.1016/j.quaint.2011.08.022.

Lane, C.S., Lowe, D.J., Blockley, S.P.E., Suzuki, T., Smith, V.C., 2017. Advancing tephrochronology as a global dating tool: applications in volcanology, archaeology, and palaeoclimatic research. Quat. Geochronol. https://doi.org/10.1016/j.quageo.2017.04.003.

Laury, R.L., Albritton, C.C., 1975. Geology of middle stone age archaeological sites in the main Ethiopian rift valley. Bull. Geol. Soc. Am. 86, 999–1011. https://doi.org/10.1130/0016-7606(1975)86<999:GOMSAA>2.0.CO, 2.

Le Turdu, C., Tiercelin, J.-J., Gibert, E., Travi, Y., Lezzar, K.-E., Richert, J.-P., Massault, M., Gasse, F., Bonnefille, R., Decobert, M., Gensous, B., Jeudy, V., Tamrat, E., Mohammed, M.U., Martens, K., Atnafu, B., Chernet, T., Williamson, D., Taieb, M., 1999. The Ziway–Shala lake basin system, Main Ethiopian Rift: influence of volcanism, tectonics, and climatic forcing on basin formation and sedimentation. Palaeogeogr. Palaeoclimatol. Palaeoecol. 150, 135–177. https://doi.org/10.1016/S0031-0182(98)00220-X.

Lowe, D.J., 2011. Tephrochronology and its application: a review. Quat. Geochronol. 6, 107–153. https://doi.org/10.1016/j.quageo.2010.08.003.

Lowe, David J., Pearce, N.J.G., Jorgensen, M.A., Kuehn, S.C., Tryon, C.A., Hayward, C.L., Lowe, D.J., 2017. Correlating Tephras and Cryptotephras Using Glass Compositional Analyses and Numerical and Statistical Methods: Review and Evaluation, vol. 175, pp. 1–44. https://doi.org/10.1016/j.quascirev.2017.08.003.

Lowe, J., Ramsey, C.B., Housley, R.A., Lane, C.S., Tomlinson, E.L., Stringer, C., Davies, W., Barton, N., Pollard, M., Gamble, C., Menzies, M., Rohling, E., Roberts, A., Blockley, S., Cullen, V., Grant, K., Lewis, M., MacLeod, Alison, White, D., Albert, Paul, Hardiman, M., Lee, S., Oh, A., Satow, C., Cross, J.K., Law, C.B., Todman, A., Bourne, A., Matthews, I., Müller, W., Smith, V., Wulf, S., Anghelinu, M., Antl-Weiser, W., Bar-Yosef, O., Boric, D., Boscato, P., Ronchitelli, A., Chabai, V., Veselsky, A., Uthmeier, T., Farrand, W., Gjipali, I., Ruka, R., Güleç, E., Karavanic, I., Karkanas, P., King, T., Komšo, D., Koumouzelis, M., Kyparissi, N., Lengyel, G., Mester, Z., Neruda, P., Panagopoulou, E., Shalamanov-Korobar, L., Tolevski, I., Sirakov, N., Guadelli, A., Guadelli, J.L., Ferrier, C., Skrdla, P., Slimak, L., Soler, N., Soler, J., Soressi, M., Tushabramishvilii, N., Zilhão, J., Angelucci, D., Albert, P., Bramham Law, C., Cullen, V.L., Lincoln, P., Staff, R., Flower, K., Aouadi-Abdeljaouad, N., Belhouchet, L., Barker, G., Bouzouggar, A., Van Peer, P., Kindermann, K., Gerken, K., Niemann, H., Tipping, R., Saville, A., Ward, T., Clausen, I., Weber, M.J., Kaiser, K., Torksdorf, J.F., Turner, F., Veil, S., Nygaard, N., Pyne-O'Donnell, S.D.F., Masojc, M., Nalepka, D., Jurochnik, A., Kabacinski, J., Antoine, P., Olive, M., Christensen, M., Bodu, P., Debout, G., Orliac, M., De Bie, M., Van Gils, M., Paulissen, E., Brou, L., Leesch, D., Hadorn, P., Thew, N., Riede, F., Heinen, M., Joris, O., Richter, J., Uthmeier, T., Knipping, M., Stika, H.P., Friedrich, M., Conard, N., Malina, M., Kind, C.J., Beutelspacher, T., Mortensen, M.F., Burdukiewicz, J.M., Szynkiewicz, A., Poltowicz-Bobak, M., Bobak, D., Wisniewski, A., Przezdziecki, M., Valde-Nowak, P., Muzyczuk, A., Bramham Law, C., Cullen, V.L., Davies, L., Lincoln, P., MacLeod, A., Morgan, P., Aydar, E., çubukçu, E., Brown, R., Coltelli, M., Castro, D., Lo Cioni, R., DeRosa, R., Donato, P., Roberto, A., Di Gertisser, R., Giordano, G., Branney, M., Jordan, N., Keller, J., Kinvig, H., Gottsman, J., Blundy, J., Marani, M., Orsi, G., Civetta, L., Arienzo, I., Carandente, A., Rosi, M., Zanchetta, G., Seghedi, I., Szakacs, A., Sulpizio, R., Thordarson, T., Trincardi, F., Vigliotti, L., Asioli, A., Piva, A., Andric, M., Brauer, A., de Klerk, P., Filippi, M.L., Finsinger, W., Galovic, L., Jones, T., Lotter, A., Müller, U., Pross, J., Mangerud, J., Lohne Pyne-O'Donnell, S., Markovic, S., Pini, R., Ravazzi, C., Riede, F., TheuerKauf, M., Tzedakis, C., Margari, V., Veres, D., Wastegård, S., Ortiz, J.E., Torres, T., Díaz-Bautista, A., Moreno, A., Valero-Garcés, B., Lowick, S., Ottolini, L., 2015. The RESET project: constructing a European tephra lattice for refined synchronisation of environmental and archaeological events during the last c. 100 ka. Quat. Sci. Rev. 118, 1–17. https://doi.org/10.1016/j.quascirev.2015.04.006.

Mana, S., DiMaggio, E., Abstracts, K.F.-A.F.M., 2018. undefined, n.d. East African Rift Tephra Database : a compilation documenting and analyzing explosive volcanism in East Africa. ui.adsabs.harvard.edu.

McDougall, I., Brown, F.H., Fleagle, J.G., 2005. Stratigraphic placement and age of modern humans from Kibish, Ethiopia. Nature 433, 733–736. https://doi.org/10.1038/nature03258.

Millard, A.R., 2008. A critique of the chronometric evidence for hominid fossils: I. Africa and the Near East 500-50 ka. J. Hum. Evol. 54, 848–874. https://doi.org/10.1016/j.jhevol.2007.11.002.

Mohr, Paul, 1966. Chabbi volcano (ethiopia). Bull. Volcanol. 29 (1), 797–815.

Mohr, P., Mitchell, J.G., Raynolds, R.G.H., 1980. Quaternary volcanism and faulting at O'A caldera, central ethiopian rift. Bull. Volcanol. 43, 173–189. https://doi.org/10.1007/BF02597619.

Mohr, P.A., Wood, C.A., 1976. Volcano spacings and lithospheric attenuation in the eastern rift of Africa. Earth Planet Sci. Lett. 33, 126–144. https://doi.org/10.1016/0012-821X(76)90166-7.

Morgan, L., Renne, P., 2008. Diachronous dawn of Africa's middle stone age: new

40Ar/39Ar ages from the Ethiopian rift. Geology 36, 967–970.

Nagaoka, S., Katoh, S., WoldeGabriel, G., Hiroshi, S., Hideo, N., Yonas, B., Gen, S., 2005. Lithostratigraphy and sedimentary environments of the hominid-bearing Pliocene–Pleistocene Konso formation in the southern main Ethiopian rift, Ethiopia. Palaeogeogr. Palaeoclimatol. Palaeoecol. 216, 333–357. https://doi.org/10.1016/j.palaeo.2004.11.008.

Niespolo, E.M., Rutte, D., Deino, A.L., Renne, P.R., 2017. Intercalibration and age of the Alder Creek sanidine 40Ar/39Ar standard. Quat. Geochronol. 39, 205–213. https://doi.org/10.1016/j.quageo.2016.09.004.

Oppenheimer, C., 2011. Eruptions that Shook the World. Cambridge University Press, Cambridge. https://doi.org/10.1017/CBO9780511978012.

Oppenheimer, C., Khalidi, L., Gratuze, B., Iverson, N., Lane, C., Vidal, C., Sahle, Y., Blegen, N., Yohannes, E., Donovan, A., Goitom, B., Hammond, J.O.S., Keall, E., Ogubazghi, G., McIntosh, B., Büntgen, U., 2019. Risk and reward: explosive eruptions and obsidian lithic resource at Nabro volcano (Eritrea). Quat. Sci. Rev. 226. https://doi.org/10.1016/j.quascirev.2019.105995.

Pearce, N., Abbott, P., 2014. Microbeam methods for the analysis of glass in fine-grained tephra deposits: a SMART perspective on current and future trends. Soc. Lond. Spec.

Peccerillo, A., Barberio, M.R., Yirgu, G., Ayalew, D., Barbieri, M., Wu, T.W., 2003. Relationships between mafic and peralkaline silicic magmatism in continental rift settings: a petrological, geochemical and isotopic study of the Gedemsa volcano, central Ethiopian rift. J. Petrol. 44, 2003–2032. https://doi.org/10.1093/petrology/egg068.

Pyle, D.M., 1999. Widely dispersed quaternary tephra in Africa. Global Planet. Change 21, 95–112. https://doi.org/10.1016/S0921-8181(99)00009-0.

Rampey, M.L., Oppenheimer, C., Pyle, D.M., Yirgu, G., 2014. Physical volcanology of the Gubisa formation, Kone volcanic complex, Ethiopia. J. Afr. Earth Sci. 96, 212–219. https://doi.org/10.1016/j.jafrearsci.2014.04.009.

Rampey, M.L., Oppenheimer, C., Pyle, D.M., Yirgu, G., 2010. Caldera-forming eruptions of the quaternary Kone volcanic complex, Ethiopia. J. Afr. Earth Sci. 58, 51–66. https://doi.org/10.1016/j.jafrearsci.2010.01.008.

Rapprich, V, et al., 2016. Wendo Koshe Pumice: the latest Holocene silicic explosive eruption product of the Corbetti volcanic system (southern Ethiopia). J. Volcanol. Geoth. Res. 310, 159–171.

Renne, P.R., Balco, G., Ludwig, K.R., Mundil, R., Min, K., 2011. Response to the comment by W.H. Schwarz et al. on "Joint determination of 40K decay constants and 40Ar*/40K for the Fish Canyon sanidine standard, and improved accuracy for 40Ar/39Ar geochronology" by P.R. Renne et al. (2010). Geochem. Cosmochim. Acta 75, 5097–5100. https://doi.org/10.1016/j.gca.2011.06.021.

Resom, A., Asrat, A., Gossa, T., Hovers, E., 2018. Petrogenesis and depositional history of felsic pyroclastic rocks from the Melka Wakena archaeological site-complex in South central Ethiopia. J. Afr. Earth Sci. 142, 93–111. https://doi.org/10.1016/j.jafrearsci.2018.03.003.

Roberts, H.M., Ramsey, C.B., Chapot, M.S., Deino, A.L., Lane, C.S., Vidal, C., Asrat, A., Cohen, A., Foerster, V., Lamb, H.F., Schäbitz, F., Trauth, M.H., Viehberg, F.A., 2021. Using multiple chronometers to establish a long, directly-dated lacustrine record: constraining >600,000 years of environmental change at Chew Bahir, Ethiopia. Quat. Sci. Rev. 266, 107025. https://doi.org/10.1016/J.QUASCIREV.2021.107025.

Romano, P., Charles White, J., Rotolo, S.G., Jordan, N.J., Cirrincione, R., De Giorgio, G., Fiannacca, P., Vaccaro, E., 2022. Contrasting styles of inter-caldera volcanism in a peralkaline system: case studies from Pantelleria (Sicily channel, Italy), 2022 Miner 12. https://doi.org/10.3390/MIN12040406, 406 12, 406.

Rooney, T.O., Furman, T., Yirgu, G., Ayalew, D., 2005. Structure of the Ethiopian lithosphere: Xenolith evidence in the main Ethiopian rift. Geochem. Cosmochim. Acta 69, 3889–3910. https://doi.org/10.1016/j.gca.2005.03.043.

Rooney, Tyrone O., Hart, William K., Hall, Chris M., Ayalew, D., Ghiorso, Mark S., Hidalgo, P., Yirgu, G., Rooney, T.O., Hidalgo, Á.P., Hart, W.K., Hall, C.M., Ayalew, Á., Yirgu, D.G., Ghiorso, M.S., 2012. Peralkaline magma evolution and the tephra record in the Ethiopian Rift. Contrib. Mineral. Petrol. 164, 407–426. https://

doi.org/10.1007/s00410-012-0744-6.

Sahle, Y., Morgan, L.E., Braun, D.R., Atnafu, B., Hutchings, W.K., 2014. Chronological and behavioral contexts of the earliest middle stone age in the gademotta formation, main ethiopian rift. Quat. Int. 331, 6–19. https://doi.org/10.1016/j.quaint.2013.03.010.

Siegburg, M., Gernon, T.M., Bull, J.M., Keir, D., Barfod, D.N., Taylor, R.N., Abebe, B., Ayele, A., 2018. Geological evolution of the Boset-Bericha volcanic complex, main Ethiopian rift: 40Ar/39Ar evidence for episodic Pleistocene to Holocene volcanism. J. Volcanol. Geoth. Res. 351, 115–133. https://doi.org/10.1016/J.JVOLGEORES.2017.12.014.

Tadesse, A.Z., Ayalew, D., Pik, R., Yirgu, G., Fontijn, K., 2019. Magmatic evolution of the Boku volcanic complex, main Ethiopian rift. J. Afr. Earth Sci. 149, 109–130. https://doi.org/10.1016/J.JAFREARSCI.2018.08.003.

Tadesse, A.Z., Fontijn, K., Melaku, A.A., Gebru, E.F., Smith, V.C., Tomlinson, E., Barfod, D., Gopon, P., Bégué, F., Caricchi, L., Laha, P., Terryn, H., Gudbrandsson, S., Yirgu, G., Ayalew, D., 2022. Eruption frequency and magnitude in a geothermally active continental rift: the Bora-Baricha-Tullu Moye volcanic complex, Main Ethiopian Rift. J. Volcanol. Geoth. Res. 423, 107471. https://doi.org/10.1016/J.JVOLGEORES.2022.107471.

Thrall, R., 1973. Gadamsa caldera, Ethiopia. Bull. Geophys. Obs. Haile Sellassie I Univ. Addis Ababa 15, 71–81.

Tomlinson, E.L., Thordarson, T., Müller, W., Thirlwall, M., Menzies, M.a., 2010a. Microanalysis of tephra by LA-ICP-MS — strategies, advantages and limitations assessed using the Thorsmörk ignimbrite (Southern Iceland). Chem. Geol. 279, 73–89. https://doi.org/10.1016/j.chemgeo.2010.09.013.

Tomlinson, E.L., Thordarson, T., Müller, W., Thirlwall, M., Menzies, M.A., 2010b. Microanalysis of tephra by LA-ICP-MS - strategies, advantages and limitations assessed using the Thorsmörk ignimbrite (Southern Iceland). Chem. Geol. 279, 73–89. https://doi.org/10.1016/j.chemgeo.2010.09.013.

Trauth, 2021. Recurring types of variability and transitions in the~ 620 kyr record of climate change from the Chew Bahir basin, southern Ethiopia. Quat. Sci. Rev. 206, 106777.

Trauth, M.H., Asrat, A., Duesing, W., Foerster, V., Kraemer, K.H., Marwan, N., Maslin, M.A., Schaebitz, F., 2019. Classifying past climate change in the Chew Bahir basin, southern Ethiopia, using recurrence quantification analysis. Clim. Dynam. 53, 2557–2572. https://doi.org/10.1007/s00382-019-04641-3.

Trauth, M.H., Foerster, V., Junginger, A., Asrat, A., Lamb, H.F., Schaebitz, F., 2018. Abrupt or gradual? Change point analysis of the late Pleistocene–Holocene climate record from Chew Bahir, southern Ethiopia. Quat. Res. 90, 321–330. https://doi.org/10.1017/qua.2018.30.

Vidal, C., Lane, C., Asrat, A., Barfod, D., Tomlinson, E., Tadesse, A.Z., Yirgu, G., Deino, A., Center, B.G., Hutchison, W., n.d. Age of the oldest Homo sapiens from eastern Africa. Nature. https://doi.org/10.21203/rs.3.rs-373661/v1Pubmed Partial Author articletitle stitle stitle Volume.

Vidal, C.M., Lane, C.S., Asrat, A., Barfod, D.N., Mark, D.F., Tomlinson, E.L., Tadesse, A.Z., Yirgu, G., Deino, A., Hutchison, W., Mounier, A., Oppenheimer, C., 2022. Age of the oldest known Homo sapiens from eastern Africa. Nat 579–583. https://doi.org/10.1038/s41586-021-04275-8, 2022 6017894 601.

Viehberg, F.A., Just, J., Dean, J.R., Wagner, B., Franz, S.O., Klasen, N., Kleinen, T., Ludwig, P., Asrat, A., Lamb, H.F., Rethemeyer, J., Milodowski, A.E., Claussen, M., Schäbitz, F., 2018. Environmental change during MIS4 and MIS 3 opened corridors in the Horn of Africa for Homo sapiens expansion. Quat. Sci. Rev. 202, 139–153. https://doi.org/10.1016/J.QUASCIREV.2018.09.008.

Williams, F.M., Williams, M.A.J., Aumento, F., 2004. Tensional fissures and crustal extension rates in the northern part of the Main Ethiopian Rift. J. Afr. Earth Sci. 38, 183–197. https://doi.org/10.1016/j.jafrearsci.2003.10.007.

Woldegabriel, G., Aronson, J., Walter, R.C., 1990. Geology, geochronology, and rift basin development in the central sector of the Main Ethiopia Rift. Geol. Soc. Am. Bull. 102, 439–458. https://doi.org/10.1130/0016-7606(1990)102<0439:GGARBD>2.3.CO;2.